Chapter 6
Developments of Mixed and Problem-Adapted BEM-Based FEM

In the final chapter some extensions and improvements of the BEM-based FEM are discussed which have not been addressed so far. In particular, the focus lies on two topics: The use of the method within mixed finite element formulations and the generalization of the construction of basis functions to polyhedral elements with polygonal faces in 3D with an application to convection-dominated problems.

The challenge in the treatment of mixed formulations is the proper construction of a $\mathbf{H}(\mathrm{div})$-conforming, vector valued approximation space over polytopal discretizations. In contrast to the previous definitions of basis functions, the construction involves local Neumann problems, which are treated in the numerical realization by appropriate boundary element methods.

The forthcoming generalization to 3D gives a H^1-conforming discretization once more which makes use of a hierarchical construction of basis functions. This adapted construction shows in particular advantageous properties when applied to convection-diffusion-reaction problems in the convection-dominated regime. The experiments indicate an improved resolution of exponential layers at outflow boundaries for the proposed approach when compared to the Streamline Upwind/Petrov-Galerkin (SUPG) method.

6.1 Mixed Formulations Treated by Means of BEM-Based FEM

Mixed finite element methods have been instrumental in the development of flexible and accurate approximations of elliptic problems with heterogeneous coefficient on triangular and rectangular grids. The flexibility can even be improved when using polygonal and polyhedral meshes. Such general cells are very desirable in many applications, e.g. flows in heterogeneous porous media as models in hydrology and

S. Weißer, *BEM-based Finite Element Approaches on Polytopal Meshes*,
Lecture Notes in Computational Science and Engineering 130,
https://doi.org/10.1007/978-3-030-20961-2_6

reservoir simulation. Therefore, a variety of approximation and solution methods on general grids, such as mixed finite element methods [120], mimetic finite difference methods [27] and the virtual element methods [29, 30, 42], have been considered, studied, and tested in the last decade. This issue has also been addressed for generalized barycentric coordinates, see [85, 166].

The goal of this section is to introduce a mixed formulation for the BEM-based FEM which has been proposed in [73]. The key idea is to construct a finite dimensional approximation space by implicitly defined basis functions which satisfy certain Neumann boundary value problems on a local, element-by-element-wise level. These problems are treated once more by means of boundary integral formulations which are discretized by boundary element methods.

Since these ideas are applied to the mixed formulation of the problem, we need a suitable discretization of the vector valued Sobolev space

$$\mathbf{H}(\mathrm{div}, \Omega) = \{\mathbf{v} \in \mathbf{L}_2(\Omega) : \mathrm{div}\ \mathbf{v} \in L_2(\Omega)\}$$

on polytopal meshes. This is done by implicitly generating trial functions. A construction of suitable trial function for the mixed FEM on polygonal meshes was done by Kuznetsov and Repin in [120] by using subdivision of the polygonal cell into triangular elements and subsequently generating the test functions locally by mixed FEM. Also similar ideas were implemented in the mixed multiscale finite element method [56, 72]. The novelty in our approach is that instead of treating the local problem by the classical mixed FEM (as in [120]) or by the multiscale FEM (as in [56]) the local problems are treated by means of boundary element methods. Thus, we avoid an additional triangulation of the elements.

6.1.1 Mixed Formulation

We consider the classical model problem of Darcy flow in a porous medium in two-dimensions. Let $\Omega \subset \mathbb{R}^2$ be a convex polygonal domain which is bounded, and let $\mathbf{n}$ be the outer unit normal vector to its boundary $\Gamma = \partial\Omega$. The boundary $\Gamma = \Gamma_D \cup \Gamma_N$ is divided into Γ_D (with non vanishing length) and Γ_N, where Dirichlet and Neumann data is prescribed, respectively. For a given source function $f \in L_2(\Omega)$ and Dirichlet data $g_D \in H^{1/2}(\Gamma_D)$, the boundary value problem for the pressure variable $p \in H^1(\Omega)$ reads

$$\begin{aligned} -\mathrm{div}(A\nabla p) &= f \quad && \text{in } \Omega\ , \\ \mathbf{n} \cdot A\nabla p &= 0 \quad && \text{on } \Gamma_N\ , \\ p &= g_D \quad && \text{on } \Gamma_D\ , \end{aligned} \tag{6.1}$$

where the tensor $A \in L_\infty(\Omega)$ represents the permeability of the medium. We assume that $A(\cdot) \in \mathbb{R}^{2\times 2}$ is symmetric, positive definite with

$$0 < a_{\min} \le \frac{\mathbf{v}^\top A(\mathbf{x})\mathbf{v}}{\mathbf{v}^\top \mathbf{v}} \le a_{\max} \quad \forall \mathbf{v} \in \mathbb{R}^2 \setminus \{0\} \quad \text{for almost all } \mathbf{x} \in \Omega$$

for constants $a_{\min}$ and $a_{\max}$, and piecewise constant with respect to the polygonal mesh later on. Vector valued Lebesgue and Sobolev spaces are indicated by bold letters. We further assume that every interior angle at any transient point between the boundary Γ_D and Γ_N is less than π, so that the solution of (6.1) with $A = I$, $f = 0$ and $g_D = 0$ is in the space $H^s(\Omega)$, $s > \frac{3}{2}$, see [87].

Next, a new unknown flux variable $\mathbf{u} = A\nabla p$ is introduced and the boundary value problem is presented as a system of first order differential equations:

$$\begin{aligned} -\operatorname{div} \mathbf{u} &= f && \text{in } \Omega \ , \\ A\nabla p &= \mathbf{u} && \text{in } \Omega \ , \\ \mathbf{n}\cdot\mathbf{u} &= 0 && \text{on } \Gamma_N \ , \\ p &= g_D && \text{on } \Gamma_D \ . \end{aligned} \tag{6.2}$$

This yields the following variational formulation in mixed form, which is actually a saddle point problem:

$$\begin{aligned} &\text{Find } (\mathbf{u}, p) \in \mathbf{H}_N(\operatorname{div}, \Omega) \times L_2(\Omega) : \\ &a(\mathbf{u}, \mathbf{v}) + b(\mathbf{v}, p) = (\mathbf{n}\cdot\mathbf{v}, g_D)_{L_2(\Gamma_D)} \quad \forall \mathbf{v} \in \mathbf{H}_N(\operatorname{div}, \Omega) \ , \\ &b(\mathbf{u}, q) = -(f, q)_{L_2(\Omega)} \quad \forall q \in L_2(\Omega) \ , \end{aligned} \tag{6.3}$$

where

$$a(\mathbf{u}, \mathbf{v}) = (A^{-1}\mathbf{u}, \mathbf{v})_{\mathbf{L}_2(\Omega)} \ , \qquad b(\mathbf{v}, q) = (\operatorname{div} \mathbf{v}, q)_{L_2(\Omega)}$$

and

$$\mathbf{H}_N(\operatorname{div}, \Omega) = \{\mathbf{v} \in \mathbf{L}_2(\Omega) : \operatorname{div} \mathbf{v} \in L_2(\Omega) \text{ and } \mathbf{n}\cdot\mathbf{v} = 0 \text{ on } \Gamma_N\} \ .$$

The space $\mathbf{H}(\operatorname{div}, \Omega)$ is equipped with the norm

$$\|\mathbf{v}\|^2_{\mathbf{H}(\operatorname{div},\Omega)} = \|\mathbf{v}\|^2_{\mathbf{L}_2(\Omega)} + \|\operatorname{div} \mathbf{v}\|^2_{L_2(\Omega)} \ .$$

It is easily seen that the bilinear forms $a(\cdot,\cdot)$ and $b(\cdot,\cdot)$ are bounded, i.e.

$$\begin{aligned} |a(\mathbf{u}, \mathbf{v})| &\le \varrho_1 \|\mathbf{u}\|_{\mathbf{H}(\operatorname{div},\Omega)} \|\mathbf{v}\|_{\mathbf{H}(\operatorname{div},\Omega)} && \text{for } \mathbf{u}, \mathbf{v} \in \mathbf{H}(\operatorname{div}, \Omega) \ , \\ |b(\mathbf{v}, q)| &\le \varrho_2 \|\mathbf{v}\|_{\mathbf{H}(\operatorname{div},\Omega)} \|q\|_{L_2(\Omega)} && \text{for } \mathbf{v} \in \mathbf{H}(\operatorname{div}, \Omega), q \in L_2(\Omega) \ , \end{aligned}$$

with some constants $\rho_1, \rho_2 > 0$. Let us set

$$\mathbf{Z} = \{\mathbf{v} \in \mathbf{H}_N(\mathrm{div}, \Omega) : \ b(\mathbf{v}, q) = 0 \ \ \forall q \in L_2(\Omega)\} \ .$$

Obviously, we have for $\mathbf{v} \in \mathbf{Z}$ that div $\mathbf{v} = 0$ and hence, the bilinear form $a(\cdot, \cdot)$ is $\mathbf{Z}$-elliptic, i.e., there exists a constant $\alpha > 0$ such that

$$a(\mathbf{v}, \mathbf{v}) \geq \alpha \|\mathbf{v}\|^2_{\mathbf{H}(\mathrm{div}, \Omega)} \quad \text{for } \mathbf{v} \in \mathbf{Z} \ .$$

Furthermore, the form $b(\cdot, \cdot)$ satisfies the so called inf-sup condition, i.e., there exists another constant $\beta > 0$ such that

$$\inf_{q \in L_2(\Omega)} \sup_{\mathbf{v} \in \mathbf{H}_N(\mathrm{div}, \Omega)} \frac{b(\mathbf{v}, q)}{\|\mathbf{v}\|_{\mathbf{H}(\mathrm{div}, \Omega)} \|q\|_{L_2(\Omega)}} \geq \beta \ .$$

Consequently, the Babuska–Brezzi theory [43] is applicable and thus, the saddle point problem (6.3) has a unique solution.

Next, we discuss the approximation of the mixed variational formulation (6.3) with the help of BEM-based FEM on polygonal meshes. Therefore, we first need to introduce a $\mathbf{H}$(div)-conforming approximation space.

6.1.2 $\mathbf{H}$(div)-*Conforming Approximation Space*

The construction of an approximation space for $L_2(\Omega)$ is rather easy, later on we use

$$M_h = \{q \in L_2(\Omega) : q|_K = const \ \forall K \in \mathscr{K}_h\} \tag{6.4}$$

for this purpose. We concentrate in this section on the definition of a conforming approximation space for $\mathbf{H}(\mathrm{div}, \Omega)$. We consider a regular and stable polygonal mesh $\mathscr{K}_h$ according to Sect. 2.2. The finite dimensional subspace of $\mathbf{H}(\mathrm{div}, \Omega)$ that serves as approximation space is defined through its basis. We restrict ourselves to the lowest order method in which the basis functions are associated with edges only. For $E \in \mathscr{E}_h$, let $\mathbf{n}_E$ be a unit normal vector, which is considered to be fixed in the sequel. Furthermore, let K_1 and K_2 be the two adjacent elements sharing the common edge E with the outer normal vectors $\mathbf{n}_{K_1}$ and $\mathbf{n}_{K_2}$, respectively. The function ϕ_E is defined implicitly as solution of the following local boundary value problem

$$\begin{aligned} &\mathrm{div}(A \nabla \phi_E) = \kappa_E(K)/|K| \quad \text{in } K \in \{K_1, K_2\} \ , \\ &\mathbf{n}_E \cdot A \nabla \phi_E = \begin{cases} h_E^{-1} & \text{on } E \ , \\ 0 & \text{on all other edges} \ , \end{cases} \end{aligned} \tag{6.5}$$

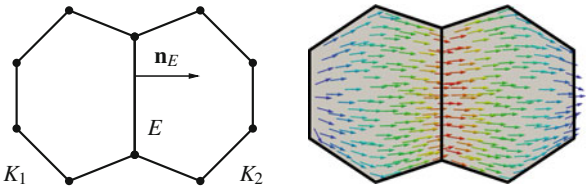

Fig. 6.1 Adjacent elements to E for the definition of ϕ_E (left) and vector field ψ_E (right)

see Fig. 6.1. Here, $\kappa_E(K) = \mathbf{n}_E \cdot \mathbf{n}_K = \pm 1$, such that the solvability condition for the Neumann problem is satisfied and (6.5) has a weak solution $\phi_E \in H^1(\Omega)$ which is unique up to an additive constant. For $E \in \mathscr{E}(K_1) \cap \mathscr{E}(K_2)$, we define

$$\psi_E(\mathbf{x}) = \begin{cases} A\nabla\phi_E(\mathbf{x}) & \text{for } \mathbf{x} \in \overline{K}_1 \cup \overline{K}_2 \,, \\ 0 & \text{else} \,. \end{cases} \tag{6.6}$$

Due to this definition one easily concludes that

$$\|\psi_E\|_{\mathbf{L}_2(K_1 \cup K_2)} = \|\nabla\phi_E\|_{\mathbf{L}_2(K_1 \cup K_2)} \leq c \,, \tag{6.7}$$

cf. also [51]. By construction, ψ_E has continuous normal flux across E and zero normal flux along all other internal edges of Ω so that $\psi_E \in \mathbf{H}(\mathrm{div}, \Omega)$. An edge $E \subset \Gamma_D$ has only one neighbouring element K, and therefore the basis function is constructed in the same way by considering problem (6.5) solely on K.

We set the finite dimensional approximation space as

$$\mathbf{X}_h = \mathrm{span}\,\{\psi_E : E \in \mathscr{E}_h\} \subset \mathbf{H}(\mathrm{div}, \Omega) \,,$$

and the subspace with vanishing normal traces on Γ_N as

$$\mathbf{X}_{h,N} = \mathrm{span}\,\{\psi_E : E \in \mathscr{E}_h \setminus \mathscr{E}_{h,N}\} \subset \mathbf{H}_N(\mathrm{div}, \Omega) \,. \tag{6.8}$$

The corresponding vector valued interpolation operator

$$\pi_h : \mathbf{H}(\mathrm{div}, \Omega) \to \mathbf{X}_h$$

is defined by

$$\pi_h \mathbf{v} = \sum_{E \in \mathscr{E}_h} v_E \, \psi_E \,, \tag{6.9}$$

where

$$v_E = \int_E \mathbf{n}_E \cdot \mathbf{v} \, \mathrm{d}s_{\mathbf{x}} \quad \text{for } E \in \mathscr{E}_h \,.$$

For $\mathbf{v} \in \mathbf{H}_N(\mathrm{div}, \Omega)$ and $E \in \mathscr{E}_{h,N}$, we point out that $v_E = 0$. Consequently, the operator satisfies

$$\pi_h : \mathbf{H}_N(\mathrm{div}, \Omega) \to \mathbf{X}_{h,N} \ .$$

Recall, that the space $\mathbf{X}_h$ in general does not consist of piecewise polynomial functions. The approximation properties of the interpolation operator π_h are established below. First of all, we have the boundedness of this operator.

Lemma 6.1 *Let $\mathscr{K}_h$ be a regular and stable polygonal mesh. The interpolation operator $\pi_h : \mathbf{H}^s(\Omega) \to \mathbf{X}_h$, $s > \frac{1}{2}$, defined by (6.9) is bounded in $\mathbf{H}^s(\Omega)$. Namely, there is a constant $c > 0$ independent of $h = \max\{h_K : K \in \mathscr{K}_h\}$ such that*

$$\|\pi_h \mathbf{v}\|_{\mathbf{L}_2(\Omega)} \le c \|\mathbf{v}\|_{\mathbf{H}^s(\Omega)} \quad \textit{for } \mathbf{v} \in \mathbf{H}^s(\Omega) \ . \tag{6.10}$$

For the restriction of the interpolation operator onto an element $K \in \mathscr{K}_h$ it holds

$$\|\pi_h \mathbf{v}\|_{\mathbf{L}_2(K)} \le c \|\mathbf{v}\|_{\mathbf{H}^s(K)} \quad \textit{for } \mathbf{v} \in \mathbf{H}^s(K) \ .$$

Proof Since π_h is defined locally, it is enough to show that this estimate is valid over each element $K \in \mathscr{K}_h$. Obviously, it holds

$$\pi_h \mathbf{v}|_K = \sum_{E \in \mathscr{E}(K)} v_E \psi_E|_K \ , \quad v_E = \int_E \mathbf{n}_E \cdot \mathbf{v} \, \mathrm{d}s_{\mathbf{x}} \ ,$$

and we have

$$\|\pi_h \mathbf{v}\|^2_{\mathbf{L}_2(K)} \le c \sum_{E \in \mathscr{E}(K)} v_E^2 \, \|\psi_E\|^2_{\mathbf{L}_2(K)}$$

with a constant c depending on the number of edges $|\mathscr{E}(K)|$, which is uniformly bounded over all elements due to the stability of the mesh, see Lemma 2.7. By (6.7) we have $\|\psi_E\|_{\mathbf{L}_2(K)} \le c$ and to conclude the proof we need to bound v_E.

We rescale the finite element K to $\widehat{K}$ by using the mapping $\mathbf{x} \mapsto \widehat{\mathbf{x}} = h_K^{-1}\mathbf{x}$, cf. (2.22). Then using the trace inequality [87]

$$\|\widehat{\mathbf{w}}\|_{\mathbf{L}_2(\widehat{E})} \le c\big(\|\widehat{\mathbf{w}}\|_{\mathbf{L}_2(\widehat{K})} + |\widehat{\mathbf{w}}|_{\mathbf{H}^s(\widehat{K})}\big) \quad \text{for } \widehat{\mathbf{w}} \in \mathbf{H}^s(\widehat{K}) \ , \ s > \tfrac{1}{2}$$

on the scaled element, where $\widehat{E}$ denotes an edge of $\widehat{K}$, we get

$$\begin{aligned} v_E^2 &\le h_E \int_E |\mathbf{n}_E \cdot \mathbf{v}|^2 \, \mathrm{d}s_{\mathbf{x}} \le h_E \int_E |\mathbf{v}|^2 \, \mathrm{d}s_{\mathbf{x}} \le h_E h_K \|\widehat{\mathbf{v}}\|^2_{\mathbf{L}_2(\widehat{E})} \\ &\le c h_E h_K \Big(\|\widehat{\mathbf{v}}\|_{\mathbf{L}_2(\widehat{K})} + |\widehat{\mathbf{v}}|_{\mathbf{H}^s(\widehat{K})} \Big)^2 \le c \Big(\|\mathbf{v}\|^2_{\mathbf{L}_2(K)} + h_K^{2s} \, |\mathbf{v}|^2_{\mathbf{H}^s(K)} \Big) \quad (6.11) \\ &\le c \, \|\mathbf{v}\|^2_{\mathbf{H}^s(K)} \, , \end{aligned}$$

since $h_K \le 1$. Thus, $\|\pi_h \mathbf{v}\|^2_{\mathbf{L}_2(K)} \le c \, \|\mathbf{v}\|^2_{\mathbf{H}^s(K)}$ and after summing for $K \in \mathscr{K}_h$ we get the desired bound. □

Next, we discuss the approximation properties of the interpolation operator π_h.

Lemma 6.2 *Let $\mathscr{K}_h$ be a regular and stable mesh and $\mathbf{v} \in \mathbf{H}^s(\Omega)$, $\frac{1}{2} < s \le 1$. It holds*

$$\|\mathbf{v} - \pi_h \mathbf{v}\|_{\mathbf{H}(\mathrm{div},\Omega)} \le c h^s \, |\mathbf{v}|_{\mathbf{H}^s(\Omega)} + \inf_{q_h \in M_h} \| \mathrm{div} \, \mathbf{v} - q_h \|_{L_2(\Omega)}$$

with $h = \max\{h_K : K \in \mathscr{K}_h\}$.

Proof On $E \in \mathscr{E}_h$ the interpolant $\pi_h \mathbf{v}$ satisfies

$$\mathbf{n}_E \cdot \pi_h \mathbf{v}\big|_E = h_E^{-1} \int_E \mathbf{n}_E \cdot \mathbf{v} \, \mathrm{d}s_{\mathbf{x}} \, ,$$

and since $\mathbf{n}_K = \kappa_E(K) \mathbf{n}_E$ for $E \in \mathscr{E}(K)$, we have according to the divergence theorem

$$\int_K \mathrm{div} \, \pi_h \mathbf{v} \, \mathrm{d}\mathbf{x} = \int_{\partial K} \mathbf{n}_K \cdot \pi_h \mathbf{v} \, \mathrm{d}s_{\mathbf{x}} = \int_{\partial K} \mathbf{n}_K \cdot \mathbf{v} \, \mathrm{d}s_{\mathbf{x}} = \int_K \mathrm{div} \, \mathbf{v} \, \mathrm{d}\mathbf{x} \, .$$

Hence, $\mathrm{div} \, \pi_h \mathbf{v}$ is the L_2-projection of $\mathrm{div} \, \mathbf{v}$ into M_h. Therefore, it is

$$\| \mathrm{div} \, \mathbf{v} - \mathrm{div} \, \pi_h \mathbf{v} \|_{L_2(\Omega)} = \inf_{q_h \in M_h} \| \mathrm{div} \, \mathbf{v} - q_h \|_{L_2(\Omega)} \, ,$$

and we obtain

$$\begin{aligned} \|\mathbf{v} - \pi_h \mathbf{v}\|_{\mathbf{H}(\mathrm{div},\Omega)} &= \Big(\|\mathbf{v} - \pi_h \mathbf{v}\|^2_{\mathbf{L}_2(\Omega)} + \| \mathrm{div}(\mathbf{v} - \pi_h \mathbf{v}) \|^2_{L_2(\Omega)} \Big)^{1/2} \\ &\le \|\mathbf{v} - \pi_h \mathbf{v}\|_{\mathbf{L}_2(\Omega)} + \inf_{q_h \in M_h} \| \mathrm{div} \, \mathbf{v} - q_h \|_{L_2(\Omega)} \, . \end{aligned}$$

It remains to estimate the error of the projection π_h in the L_2-norm. We consider this term over the scaled element $\widehat{K}$ which is obtained by the mapping $\mathbf{x} \mapsto \widehat{\mathbf{x}} = h_K^{-1} \mathbf{x}$, cf. (2.22). All objects on the scaled element $\widehat{K}$ are indicated by a hat such as the

gradient operator $\widehat{\nabla}$ with respect to the variable $\widehat{\mathbf{x}}$. Furthermore, it is $\widehat{\psi}_E(\widehat{\mathbf{x}}) = \psi_E(\mathbf{x})$ and $\psi_{\widehat{E}}$ denotes the basis functions defined on $\widehat{K}$ for the edge $\widehat{E} \in \mathscr{E}(\widehat{K})$ which corresponds to $E \in \mathscr{E}(K)$. First, we show the identity $\widehat{\pi_h \mathbf{v}} = \widehat{\pi}_h \widehat{\mathbf{v}}$. To this end, we observe that

$$\psi_E(\mathbf{x}) = A\nabla\phi_E(\mathbf{x}) = A\nabla\widehat{\phi}_E(h_K^{-1}\mathbf{x}) = h_K^{-1} A\widehat{\nabla}\widehat{\phi}_E(\widehat{\mathbf{x}}) \,. \tag{6.12}$$

Furthermore, $\widehat{\phi}_E$ satisfies

$$\widehat{\operatorname{div}}\big(A\widehat{\nabla}\widehat{\phi}_E\big) = h_K^2 \operatorname{div}\big(A\nabla\phi_E\big) = \frac{\kappa_{\widehat{E}}(\widehat{K})}{|\widehat{K}|} \quad \text{in } \widehat{K} \,,$$

since $|\widehat{K}| = |K|/h_K^2$, and

$$\mathbf{n}_{\widehat{E}} \cdot A\widehat{\nabla}\widehat{\phi}_E = \mathbf{n}_E \cdot h_K A\nabla\phi_E = h_{\widehat{E}}^{-1} \quad \text{on } \widehat{E} \,,$$

since $h_{\widehat{E}} = h_E/h_K$. The basis function $\psi_{\widehat{E}} = A\widehat{\nabla}\phi_{\widehat{E}}$ on the scaled element $\widehat{K}$ is given according to (6.5) and (6.6). Obviously, $\widehat{\phi}_E$ and $\phi_{\widehat{E}}$ are solutions of the same Neumann problem on $\widehat{K}$ and consequently it is

$$\widehat{\phi}_E = \phi_{\widehat{E}} + C$$

for a constant $C \in \mathbb{R}$. Hence, (6.12) yields

$$\widehat{\psi}_E = h_K^{-1} \psi_{\widehat{E}} \,.$$

For the interpolation operator we thus get on each element $K \in \mathscr{K}_h$

$$\widehat{\pi_h \mathbf{v}} = \sum_{E \in \mathscr{E}(K)} v_E \widehat{\psi}_E = \sum_{\widehat{E} \in \mathscr{E}(\widehat{K})} v_E h_K^{-1} \psi_{\widehat{E}} = \sum_{\widehat{E} \in \mathscr{E}(\widehat{K})} v_{\widehat{E}} \psi_{\widehat{E}} = \widehat{\pi}_h \widehat{\mathbf{v}} \,,$$

because of

$$v_E = \int_E \mathbf{n}_E \cdot \mathbf{v} \, \mathrm{d}s_{\mathbf{x}} = \frac{h_E}{h_{\widehat{E}}} \int_{\widehat{E}} \mathbf{n}_{\widehat{E}} \cdot \widehat{\mathbf{v}} \, \mathrm{d}s_{\widehat{\mathbf{x}}} = h_K \, v_{\widehat{E}}$$

due to $h_{\widehat{E}} = h_E/h_K$.

With the help of Lemma 6.1 and exploiting the reverse triangle inequality, we have for $s > \frac{1}{2}$

$$\|\widehat{\mathbf{v}} - \widehat{\pi}_h \widehat{\mathbf{v}}\|_{\mathbf{L}_2(\widehat{K})} \le c \|\widehat{\mathbf{v}}\|_{\mathbf{H}^s(\widehat{K})} \,. \tag{6.13}$$

Next, in order to apply the Bramble–Hilbert Lemma, see Theorem 1.9, to the functional

$$\mathbf{f}(\widehat{\mathbf{v}}) = \|\widehat{\mathbf{v}} - \widehat{\pi}_h \widehat{\mathbf{v}}\|_{\mathbf{L}_2(\widehat{K})} ,$$

we further have to show that $\widehat{\pi}_h \mathbf{d} = \mathbf{d}$ if $\mathbf{d} = (d_1, d_2)^\top \in \mathbb{R}^2$ is a constant vector. By construction, it is $\widehat{\pi}_h \mathbf{d} = \widehat{\nabla}\phi$ over $\widehat{K}$, where ϕ is the solution of

$$-\widehat{\Delta}\phi = 0 \quad \text{in } \widehat{K} \qquad \text{and} \qquad \mathbf{n}_{\widehat{K}} \cdot \widehat{\nabla}\phi = \mathbf{n}_{\widehat{K}} \cdot \mathbf{d} \quad \text{on } \partial\widehat{K} . \tag{6.14}$$

The boundary data for this problem is compatible,

$$\int_{\partial\widehat{K}} \mathbf{n}_{\widehat{K}} \cdot \mathbf{d} \, \mathrm{d}s_{\widehat{\mathbf{x}}} = \int_{\widehat{K}} \widehat{\mathrm{div}}\, \mathbf{d} \, \mathrm{d}\widehat{\mathbf{x}} = 0 ,$$

and therefore the problem has a unique solution up to an additive constant. Obviously, $\phi(\widehat{\mathbf{x}}) = d_1\widehat{x}_1 + d_2\widehat{x}_2 + C$ satisfies (6.14) for $C \in \mathbb{R}$ and so $\widehat{\pi}_h \mathbf{d} = \widehat{\nabla}\phi = \mathbf{d}$.

Finally, the scaling and the application of the Bramble–Hilbert Lemma to the functional $\mathbf{f}$ yields

$$\|\mathbf{v} - \pi_h \mathbf{v}\|_{\mathbf{L}_2(K)} = h_K \|\widehat{\mathbf{v}} - \widehat{\pi}_h \widehat{\mathbf{v}}\|_{\mathbf{L}_2(\widehat{K})} \le c h_K |\widehat{\mathbf{v}}|_{\mathbf{H}^s(\widehat{K})} = c h_K^s |\mathbf{v}|_{\mathbf{H}^s(K)} ,$$

and after summation over all elements we obtain the desired bound. □

Remark 6.3 The constant c in Lemmata 6.1 and 6.2 only depend on the regularity and stability of the mesh. This can be seen as in [51], since the estimates in the proofs, which might incorporate additional dependencies, have only been performed on the scaled element.

6.1.3 Approximation of Mixed Formulation

By the use of the previously introduced spaces, the discrete version of the variational formulation (6.3) reads:

$$\begin{aligned} &\text{Find } (\mathbf{u}_h, p_h) \in \mathbf{X}_{h,N} \times M_h : \\ &a(\mathbf{u}_h, \mathbf{v}_h) + b(\mathbf{v}_h, p_h) = (\mathbf{n} \cdot \mathbf{v}_h, g_D)_{L_2(\Gamma_D)} \qquad \forall \mathbf{v}_h \in \mathbf{X}_{h,N} , \\ &\qquad\qquad b(\mathbf{u}_h, q_h) = -(f, q_h)_{L_2(\Omega)} \qquad\quad \forall q_h \in M_h . \end{aligned} \tag{6.15}$$

To prove unique solvability of the discrete problem, we use a fundamental theorem in the mixed finite element analysis, see [43]. This theory relies on the space

$$\mathbf{Z}_h = \{\mathbf{v}_h \in \mathbf{X}_{h,N} : b(\mathbf{v}_h, q_h) = 0 \quad \forall q_h \in M_h\}$$

and the following two assumptions.

A1: There exists a constant $\alpha^* > 0$ such that

$$a(\mathbf{v}_h, \mathbf{v}_h) \geq \alpha^* \|\mathbf{v}_h\|^2_{\mathbf{H}(\mathrm{div},\Omega)} \quad \text{for } \mathbf{v}_h \in \mathbf{Z}_h \ .$$

A2: There exists a constant $\beta^* > 0$ such that

$$\inf_{q_h \in M_h} \sup_{\mathbf{v}_h \in \mathbf{X}_{h,N}} \frac{b(\mathbf{v}_h, q_h)}{\|\mathbf{v}_h\|_{\mathbf{H}(\mathrm{div},\Omega)} \|q_h\|_{L_2(\Omega)}} \geq \beta^* \ .$$

Such assumptions hold in the continuous setting and they are used in order to prove unique solvability of the mixed formulation (6.3). In the discrete case, however, we have to verify these assumptions for the introduced approximation spaces. Afterwards, the continuity of the bilinear forms $a(\cdot,\cdot)$ on $\mathbf{X}_h \times \mathbf{X}_h$ and $b(\cdot,\cdot)$ on $\mathbf{X}_h \times M_h$ as well as A1 and A2 are sufficient for the existence and uniqueness of the solution of the discrete problem (6.15), see [43]. Furthermore, this theory gives an error estimate. Thus, Babuska–Brezzi theory yields the main result of this section.

Theorem 6.4 *The problem* (6.15) *with* $\mathbf{X}_{h,N}$ *defined by* (6.8) *and* M_h *defined by* (6.4) *has a unique solution* $(\mathbf{u}_h, p_h) \in \mathbf{X}_{h,N} \times M_h$. *Furthermore, there exists a constant c depending only on* α^*, β^*, ϱ_1 *and* ϱ_2 *as well as on the mesh regularity and stability such that*

$$\begin{aligned} &\|\mathbf{u} - \mathbf{u}_h\|_{\mathbf{H}(\mathrm{div},\Omega)} + \|p - p_h\|_{L_2(\Omega)} \\ &\qquad \leq c \left\{ \inf_{\mathbf{v}_h \in \mathbf{X}_h} \|\mathbf{u} - \mathbf{v}_h\|_{\mathbf{H}(\mathrm{div},\Omega)} + \inf_{q_h \in M_h} \|p - q_h\|_{L_2(\Omega)} \right\} . \end{aligned} \tag{6.16}$$

Proof To show existence and uniqueness we need to verify A1 and A2. Assumption A1 is shown in a straightforward manner. Since div $\mathbf{v}_h$ is constant on each element it follows

$$\mathbf{Z}_h = \{\mathbf{v}_h \in \mathbf{X}_{h,N} : \mathrm{div}\ \mathbf{v}_h = 0 \text{ in } K \in \mathscr{K}_h\} \ , \tag{6.17}$$

and therefore we get for $\mathbf{v}_h \in \mathbf{Z}_h$

$$\begin{aligned} a(\mathbf{v}_h, \mathbf{v}_h) &= \sum_{K \in \mathscr{K}_h} \int_K A^{-1} \mathbf{v}_h \cdot \mathbf{v}_h \, \mathrm{d}\mathbf{x} \\ &\geq a_{\max}^{-1} \sum_{K \in \mathscr{K}_h} \left\{ \|\mathbf{v}_h\|^2_{\mathbf{L}_2(K)} + \|\mathrm{div}\ \mathbf{v}_h\|^2_{L_2(K)} \right\} = \alpha^* \|\mathbf{v}_h\|^2_{\mathbf{H}(\mathrm{div},\Omega)} \ . \end{aligned}$$

To verify A2 we use the interpolation operator π_h defined by (6.9). We have shown that π_h satisfies (6.10). In the following we make use of an auxiliary problem.

For given $q_h \in M_h$, we consider ϕ as unique solution of the boundary value problem

$$\begin{aligned} \Delta\phi &= q_h \quad \text{in } \Omega \ , \\ \mathbf{n} \cdot \nabla\phi &= 0 \quad \text{on } \Gamma_N \ , \\ \phi &= 0 \quad \text{on } \Gamma_D \ . \end{aligned} \tag{6.18}$$

Since we have assumed that Ω is convex, it is well known that if either Γ_N or Γ_D is an empty set, then the solution of this problem belongs to $H^2(\Omega)$, see, e.g., [87]. The general case has been studied in details by Bacuta et al. [17] by the use of FEM tools. If all angles between edges with Neumann and Dirichlet data are strictly less than π, then there exists $s > \frac{1}{2}$ such that

$$\|\phi\|_{H^{1+s}(\Omega)} \le c\|q_h\|_{L_2(\Omega)} \ ,$$

cf. [17, Theorem 4.1]. Let $\mathbf{w} = \nabla\phi$. Due to the construction, $\mathbf{w}$ has a piecewise constant divergence and the normal trace of $\mathbf{w}$ vanishes on Γ_N. On each $E \in \mathscr{E}_h$ the function $\pi_h\mathbf{w}$ satisfies

$$\mathbf{n}_E \cdot \pi_h\mathbf{w}\big|_E = h_E^{-1} \int_E \mathbf{n}_E \cdot \mathbf{w} \, ds_{\mathbf{x}} \ ,$$

and since $\mathbf{n}_K = \kappa_E(K)\mathbf{n}_E$ for $E \in \mathscr{E}(K)$, we have

$$\int_K \operatorname{div} \pi_h\mathbf{w} \, d\mathbf{x} = \int_{\partial K} \mathbf{n}_K \cdot \pi_h\mathbf{w} \, ds_{\mathbf{x}} = \int_{\partial K} \mathbf{n}_K \cdot \mathbf{w} \, ds_{\mathbf{x}} = \int_K \operatorname{div} \mathbf{w} \, d\mathbf{x} \ .$$

Therefore, it is

$$\operatorname{div} \mathbf{w} = \operatorname{div} \pi_h\mathbf{w} = q_h \quad \text{for } K \in \mathscr{K}_h \ .$$

Making use of the stability of the interpolation operator π_h, see Lemma 6.1, we get

$$\|\pi_h\mathbf{v}\|_{\mathbf{L}_2(\Omega)} \le c\|\mathbf{v}\|_{\mathbf{H}^s(\Omega)} \le c\|\phi\|_{H^{1+s}(\Omega)} \le c\|q_h\|_{L_2(\Omega)} \ , \tag{6.19}$$

where $c > 0$ is a generic constant. Finally, we obtain

$$\begin{aligned} \sup_{\mathbf{v}_h \in \mathbf{X}_{h,N}} \frac{b(\mathbf{v}_h, q_h)}{\|\mathbf{v}_h\|_{\mathbf{H}(\operatorname{div},\Omega)}} &\ge \frac{b(\pi_h\mathbf{w}, q_h)}{\|\pi_h\mathbf{w}\|_{\mathbf{H}(\operatorname{div},\Omega)}} = \frac{\|q_h\|^2_{L_2(\Omega)}}{\left(\|\pi_h\mathbf{w}\|^2_{\mathbf{L}_2(\Omega)} + \|\operatorname{div}(\pi_h\mathbf{w})\|^2_{L_2(\Omega)}\right)^{1/2}} \\ &\ge \frac{\|q_h\|^2_{L_2(\Omega)}}{\left(c^2\|q_h\|^2_{L_2(\Omega)} + \|q_h\|^2_{L_2(\Omega)}\right)^{1/2}} \ge \beta^*\|q_h\|_{L_2(\Omega)} \ , \end{aligned}$$

that proves the inf-sup condition.

Following standard arguments of Babuska and Brezzi utilizing A1 and A2, it is easily shown that the discrete problem (6.15) has a unique solution and that the error estimate (6.16) holds, see, e.g., [43]. □

6.1.4 Realization and Numerical Examples

In contrast to (6.2), the following numerical examples are a little bit more general and involve non-homogeneous Neumann data, i.e. $\mathbf{n} \cdot \mathbf{u} = g_N$ on Γ_N for $g_N \in L_2(\Gamma_N)$. As usual, we seek the approximation $\mathbf{u}_h = \mathbf{u}_{h,N} + \mathbf{u}_{h,g_N}$, where $\mathbf{u}_{h,N} \in \mathbf{X}_{h,N}$ has homogeneous Neumann data and $\mathbf{u}_{h,g_N} \in \mathbf{X}_h$ is an extension of the given data g_N in the discrete space, e.g.,

$$\mathbf{u}_{h,g_N} = \sum_{E \in \mathcal{E}_{h,N}} \int_E g_N \, \mathrm{d}s_{\mathbf{x}} \, \psi_E \, .$$

The mixed formulation for the approximation reads:

$$\begin{aligned} &\text{Find } (\mathbf{u}_{h,N}, p_h) \in \mathbf{X}_{h,N} \times M_h : \\ &a(\mathbf{u}_{h,N}, \mathbf{v}_h) + b(\mathbf{v}_h, p_h) = (\mathbf{n} \cdot \mathbf{v}_h, g_D)_{L_2(\Gamma_D)} - a(\mathbf{u}_{h,g_N}, \mathbf{v}_h) \quad \forall \mathbf{v}_h \in \mathbf{X}_{h,N} \, , \\ &b(\mathbf{u}_{h,N}, q_h) = -(f, q_h)_{L_2(\Omega)} - b(\mathbf{u}_{h,g_N}, q_h) \qquad \forall q_h \in M_h \, . \end{aligned} \tag{6.20}$$

It remains to discuss the computation of the involved terms. Afterwards, the system of linear equations can be set up for the expansion coefficients of the approximations $\mathbf{u}_h$ and p_h in the form

$$\begin{pmatrix} A_h & B_h^\top \\ B_h & 0 \end{pmatrix} \begin{pmatrix} \underline{\mathbf{u}}_h \\ \underline{p}_h \end{pmatrix} = \begin{pmatrix} \underline{r}_1 \\ \underline{r}_2 \end{pmatrix} \, , \tag{6.21}$$

where A_h and B_h are the matrices given by testing the bilinear forms $a(\cdot, \cdot)$ and $b(\cdot, \cdot)$ with the basis functions of $\mathbf{X}_{h,N}$ and M_h, respectively. The vectors $\underline{r}_1$ and $\underline{r}_2$ contain the corresponding right hand sides of (6.20). The system can be solved with the favourite linear algebra algorithm. Alternatively, one might use the Schur complement. The first equation in (6.21) yields

$$\underline{\mathbf{u}}_h = A_h^{-1} \left(\underline{r}_1 - B_h^\top \underline{p}_h \right) \, ,$$

and inserting into the second equation of (6.21) gives

$$B_h A_h^{-1} B_h^\top \underline{p}_h = B_h A_h^{-1} \underline{r}_1 - \underline{r}_2$$

for the computation of $\underline{p}_h$.

6.1.4.1 Computational Realization

In this section we address the computational realization of the terms within the mixed formulation (6.20). The integrals $(f, q_h)_{L_2(\Omega)}$ and $(\mathbf{n} \cdot \mathbf{v}_h, g_D)_{L_2(\Gamma_D)}$ are rather standard. The first integral is split into its contribution over each polygonal element and then a quadrature formula is applied over the auxiliary triangulation as in (4.43). For the second integral we recognize that $\mathbf{n} \cdot \mathbf{v}_h$ is constant over each edge of the discretization. Consequently, we split the integral on Γ_D into its contributions over the single edges and apply Gaussian quadrature. We recall that div $\mathbf{v}_h$ is constant on each element for $\mathbf{v}_h \in \mathbf{X}_h$. Therefore, the entries of B_h have an analytic expression. For $\mathbf{v}_h \in \mathbf{X}_h$ and $q_h \in M_h$, we obtain

$$b(\mathbf{v}_h, q_h) = \sum_{K \in \mathscr{K}_h} |K| \ \operatorname{div} \mathbf{v}_h\big|_K \ q_h \ .$$

In order to treat the bilinear form $a(\cdot, \cdot)$, we apply boundary element techniques. We exploit the definition of the basis functions ψ_E in (6.6) with the help of ϕ_E. Obviously, the function $\mathbf{u}_h \in \mathbf{X}_h$ can be expressed locally over each element $K \in \mathscr{K}_h$ as

$$\mathbf{u}_h = A \nabla \phi_{\mathbf{u}}$$

where $\phi_{\mathbf{u}}$ is the unique solution of

$$\begin{aligned} \operatorname{div}(A \nabla \phi_{\mathbf{u}}) &= f_{\mathbf{u}} \quad \text{in } K \ , \\ \mathbf{n}_K \cdot A \nabla \phi_{\mathbf{u}} &= g_{\mathbf{u}} \quad \text{on } \partial K \ , \end{aligned} \tag{6.22}$$

with a constant $f_{\mathbf{u}}$ and piecewise constant $g_{\mathbf{u}} \in \mathscr{P}^0_{\mathrm{pw,d}}(\partial K)$. Furthermore, the function $\phi_{\mathbf{u}}$ is decomposed into $\phi_{\mathbf{u}} = \phi_{\mathbf{u},0} + \phi_{\mathbf{u},f}$ with

$$\phi_{\mathbf{u},f}(\mathbf{x}) = \tfrac{1}{4} f_{\mathbf{u}} (\mathbf{x} - \bar{\mathbf{x}}_K)^\top A^{-1} (\mathbf{x} - \bar{\mathbf{x}}_K) \in \mathscr{P}^2(K) \ ,$$

such that

$$\operatorname{div}(A \nabla \phi_{\mathbf{u},f}) = f_{\mathbf{u}} \quad \text{in } K \ , \tag{6.23}$$

and hence, $\phi_{\mathbf{u},0}$ is the solution of the Neumann problem

$$\begin{aligned} -\operatorname{div}(A \nabla \phi_{\mathbf{u},0}) &= 0 && \text{in } K \ , \\ \mathbf{n}_K \cdot A \nabla \phi_{\mathbf{u},0} &= g_{\mathbf{u}} - \mathbf{n}_K \cdot A \nabla \phi_{\mathbf{u},f} && \text{on } \partial K \ . \end{aligned} \tag{6.24}$$

The function $\phi_{\mathbf{u},0}$ is unique up to an additive constant. A small exercise shows that $g_{\mathbf{u}} - \mathbf{n}_K \cdot A \nabla \phi_{\mathbf{u},f} \in \mathscr{P}^0_{\mathrm{pw,d}}(\partial K)$, since the gradient of a quadratic function is

linear and since the normal component of a linear function along a straight edge is constant. In the case of a scalar valued diffusion coefficient $A \in \mathbb{R}$, we apply the discussed boundary element method from Chap. 4 for the Neumann problem of the Laplace equation. But, there is also a boundary element method available for a general, symmetric and positive definite matrix $A \in \mathbb{R}^{2\times 2}$, see [151]. We comment on this in Sect. 6.2.3.

Consequently, we have the tools to approximate the Dirichlet trace of $\phi_{\mathbf{u},0}$ on ∂K and we utilize the representation formula to evaluate $\phi_{\mathbf{u},0}$ and its derivatives inside the elements. This allows for a very accurate approximation of $\mathbf{u}_h$ inside K. Thus, we have different possibilities to treat the bilinear form $a(\cdot,\cdot)$ as in Sect. 4.5. Either we use a numerical integration scheme over the polygonal elements and evaluate $\mathbf{u}_h$ and $\mathbf{v}_h$ with the help of the representation formula in the quadrature nodes, or we utilize partial integration locally in order to reformulate the volume integrals into boundary integrals. The first strategy is analog to the volume quadrature in (4.43). For the second strategy we write

$$\mathbf{u}_h = A\nabla\phi_{\mathbf{u}} \qquad \text{and} \qquad \mathbf{v}_h = A\nabla\phi_{\mathbf{v}}$$

with

$$\phi_{\mathbf{u}} = \phi_{\mathbf{u},0} + \phi_{\mathbf{u},f} \qquad \text{and} \qquad \phi_{\mathbf{v}} = \phi_{\mathbf{v},0} + \phi_{\mathbf{v},f}$$

as above. This decomposition and the symmetry of A yield

$$\begin{aligned} a(\mathbf{u}_h,\mathbf{v}_h) &= \sum_{K\in\mathscr{K}_h} \left(A^{-1}\mathbf{u}_h,\mathbf{v}_h\right)_{\mathbf{L}_2(K)} = \sum_{K\in\mathscr{K}_h} (A\nabla\phi_{\mathbf{u}},\nabla\phi_{\mathbf{v}})_{\mathbf{L}_2(K)} \\ &= \sum_{K\in\mathscr{K}_h} \Big\{ \left(A\nabla\phi_{\mathbf{u},0},\nabla\phi_{\mathbf{v},0}\right)_{\mathbf{L}_2(K)} + \left(A\nabla\phi_{\mathbf{u},f},\nabla\phi_{\mathbf{v},f}\right)_{\mathbf{L}_2(K)} \\ &\qquad + \left(A\nabla\phi_{\mathbf{u},0},\nabla\phi_{\mathbf{v},f}\right)_{\mathbf{L}_2(K)} + \left(\nabla\phi_{\mathbf{u},f},A\nabla\phi_{\mathbf{v},0}\right)_{\mathbf{L}_2(K)} \Big\} \\ &= \sum_{K\in\mathscr{K}_h} \Big\{ I + II + III + IV \Big\} . \end{aligned}$$

The terms I–IV are treated separately employing integration by parts and the properties (6.23) and (6.24). We obtain

$$III = \left(\mathbf{n}_K \cdot A\nabla\phi_{\mathbf{u},0},\phi_{\mathbf{v},f}\right)_{L_2(\partial K)} \qquad \text{and} \qquad IV = \left(\mathbf{n}_K \cdot A\nabla\phi_{\mathbf{v},0},\phi_{\mathbf{u},f}\right)_{L_2(\partial K)} ,$$

and consequently the terms are given as integrals of piecewise quadratic polynomials over ∂K that are computed analytically. The same arguments yield

$$II = \left(\mathbf{n}_K \cdot A\nabla\phi_{\mathbf{u},f},\phi_{\mathbf{v},f}\right)_{L_2(\partial K)} - \left(f_{\mathbf{u}},\phi_{\mathbf{v},f}\right)_{L_2(K)}$$

with an integral of a piecewise quadratic polynomial over the boundary ∂K and an integral of a quadratic polynomial over K, since $f_{\mathbf{u}}$ is constant. Both integrals are computed analytically, where we apply the divergence theorem to transform the volume integral to a boundary integral. Finally, I has the form

$$I = \left(\mathbf{n}_K \cdot A\nabla\phi_{\mathbf{u},0}, \phi_{\mathbf{v},0}\right)_{L_2(\partial K)}$$

after integration by parts. Here, $\mathbf{n}_K \cdot A\nabla\phi_{\mathbf{u},0}$ is a piecewise constant function on ∂K and $\phi_{\mathbf{v},0}$ is treated by means of boundary element methods as discussed in Chap. 4. For scalar valued diffusion $A \in \mathbb{R}$, we obtain with the notation of trace and boundary integral operators

$$I = \left(A\gamma_1^K\phi_{\mathbf{u},0}, \gamma_0^K\phi_{\mathbf{v},0}\right)_{L_2(\partial K)} = A\left(\gamma_1^K\phi_{\mathbf{u},0}, \mathbf{P}_K\gamma_1^K\phi_{\mathbf{v},0}\right)_{L_2(\partial K)} ,$$

where $\mathbf{P}_K$ denotes the Poincaré–Steklov operator (4.14), which maps the Neumann to the Dirichlet trace. Hence, I is approximated utilizing the non-symmetric

$$\mathbf{P}_{K,h}^{\text{unsym}} = \mathbf{M}_{K,h}\widetilde{\mathbf{D}}_{K,h}^{-1}\left(\tfrac{1}{2}\mathbf{M}_{K,h}^{\top} - \mathbf{K}_{K,h}^{\top}\right)$$

or the symmetric

$$\mathbf{P}_{K,h} = \mathbf{V}_{K,h} + \left(\tfrac{1}{2}\mathbf{M}_{K,h} - \mathbf{K}_{K,h}\right)\widetilde{\mathbf{D}}_{K,h}^{-1}\left(\tfrac{1}{2}\mathbf{M}_{K,h}^{\top} - \mathbf{K}_{K,h}^{\top}\right)$$

discretization of $\mathbf{P}_K$, see (4.14) as well as (4.15) and the more detailed discussion in Sect. 4.5. For matrix valued diffusion $A \in \mathbb{R}^{2\times 2}$, the Neumann trace is defined by

$$\gamma_1^K\phi_{\mathbf{u},0} = \mathbf{n}_K \cdot A\nabla\phi_{\mathbf{u},0}$$

for sufficiently regular functions and we can proceed analogously with the BEM.

6.1.4.2 Numerical Examples

To validate our theoretical findings, we give some numerical experiments for the mixed formulation of the BEM-based FEM. In the realization, we set up the matrix A_h with the brute force approach utilizing numerical integration over polygonal elements, where the test and trial functions are evaluated with the help of the representation formula. Furthermore, the system of linear equations (6.21) is solved by means of GMRES [150].

Two model problems are posed on the domain $\Omega = (-1, 1)^2$ and we decompose its boundary into

$$\Gamma_D = \{(x_1, -1)^{\top} : -1 \le x_1 \le 1\} \quad \text{and} \quad \Gamma_N = \partial\Omega \setminus \Gamma_D .$$

In the first example, we choose the data g_D and g_N in such a way that the smooth function $p(\mathbf{x}) = \exp(2\pi(x_1 - 0.3))\,\cos(2\pi(x_2 - 0.3))$, $\mathbf{x} \in \mathbb{R}^2$ is the exact solution of

$$-\Delta p = 0 \quad \text{in } \Omega\,, \qquad \mathbf{n} \cdot \nabla p = g_N \quad \text{on } \Gamma_N\,, \qquad p = g_D \quad \text{on } \Gamma_D\,.$$

Thus, $(\mathbf{u}, p)$ with $\mathbf{u} = \nabla p$ solves the corresponding mixed formulation (6.20). For the second example, we take $p(\mathbf{x}) = \sin(\pi x_1)\sin(\pi x_2)$, $\mathbf{x} \in \mathbb{R}^2$ as solution of

$$-\Delta p = f \quad \text{in } \Omega\,, \qquad \mathbf{n} \cdot \nabla p = g_N \quad \text{on } \Gamma_N\,, \qquad p = 0 \quad \text{on } \Gamma_D$$

with corresponding data f and g_N. The BEM-based FEM is applied on a sequence of honeycomb meshes consisting of hexahedral elements with decreasing mesh size h, see Fig. 6.2. We analyse numerically the relative error

$$\frac{\|\mathbf{u} - \mathbf{u}_h\|_{\mathbf{H}(\mathrm{div},\Omega)} + \|p - p_h\|_{L_2(\Omega)}}{\|\mathbf{u}\|_{\mathbf{H}(\mathrm{div},\Omega)} + \|p\|_{L_2(\Omega)}}\,. \tag{6.25}$$

According to Theorem 6.4, the interpolation error in Lemma 6.2 and known approximation properties of the space M_h, cf. Lemma 3.4, we expect linear convergence of the relative error (6.25) with respect to the mesh size $h = \max\{h_K : K \in \mathscr{K}_h\}$. The numerical experiments confirm this fact, see Fig. 6.3. In Fig. 6.4, the approximations p_h and $\mathbf{u}_h$ of the primal and the flux variable are visualized for the second problem.

In the third and final example, we consider a problem with unknown solution. Let $\Omega = (0, 1)^2$ and we prescribe Dirichlet data on the left edge of the square and Neumann data else, such that

$$\Gamma_D = \{(0, x_2)^\top : 0 \le x_2 \le 1\} \quad \text{and} \quad \Gamma_N = \partial\Omega \setminus \Gamma_D\,.$$

We choose the Dirichlet data as

$$g_D(\mathbf{x}) = 1 - x_2 \quad \text{for } \mathbf{x} \in \Gamma_D\,,$$

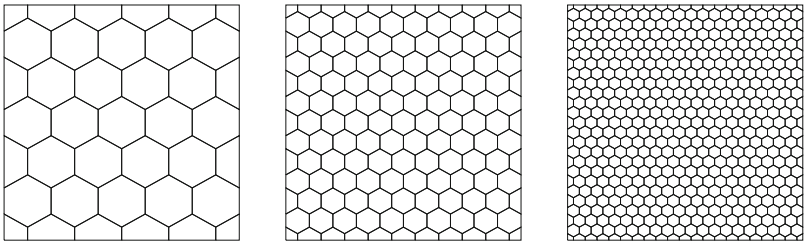

Fig. 6.2 Sequence of honeycomb meshes with hexahedral elements and decreasing mesh size h from left to right

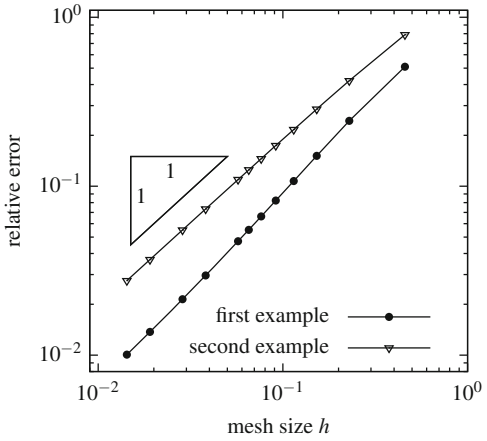

Fig. 6.3 Relative error (6.25) with respect to h in logarithmic scale for first and second example

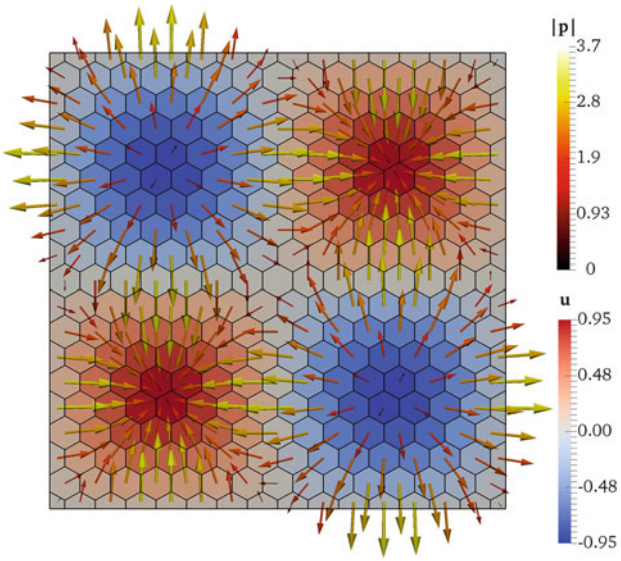

Fig. 6.4 Visualization of the approximation of the second example, the primal variable p_h and the flux unknown $\mathbf{u}_h$

and the Neumann data such that we have an inflow in the left part of the upper edge and an outflow in the lower part of the right edge, namely

$$g_N(\mathbf{x}) = \begin{cases} -3 & \text{for } 0 \le x_1 \le 1/2,\ x_2 = 1\ , \\ 3 - 3x_2 & \text{for } x_1 = 1,\ 0 \le x_2 \le 1/2\ , \\ 0 & \text{else on } \Gamma_N\ . \end{cases}$$

We consider the mixed boundary value problem

$$\begin{aligned} -\operatorname{div} \mathbf{u} &= 0 && \text{in } \Omega\ , \\ \nabla p &= \mathbf{u} && \text{in } \Omega\ , \\ \mathbf{n} \cdot \mathbf{u} &= g_N && \text{on } \Gamma_N\ , \\ p &= g_D && \text{on } \Gamma_D \end{aligned}$$

in the saddle point formulation (6.20) for the unknowns $\mathbf{u}$ and p. The approximation obtained by BEM-based FEM strategies is visualized in Fig. 6.5 on a polygonal mesh. The vector field $\mathbf{u}_h$ behaves as expected, it points form the inflow boundary towards the outflow boundary and it is almost parallel to the boundary with homogeneous Neumann data.

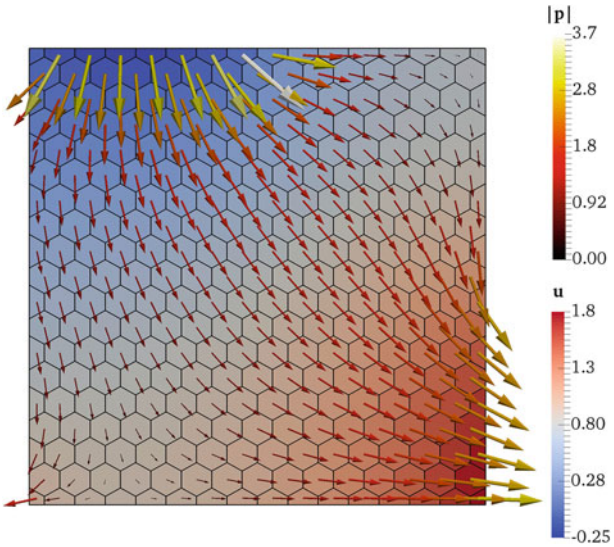

Fig. 6.5 Visualization of the approximation of third example, the primal variable p_h and the flux unknown $\mathbf{u}_h$

6.2 3D Generalization with Application to Convection-Diffusion-Reaction Equation

In this section, we discuss a generalization of a variant of the BEM-based finite element method studied so far. We address the definition of basis functions on meshes with polyhedral elements having polygonal faces. These functions are used to construct an approximation space V_h which can be utilized in the discrete Galerkin formulation of the finite element method. The idea of the BEM-based FEM is to define the basis functions implicitly on each element as local solutions of the underlying differential equation and to treat the local problems by boundary element methods. In the following, we push this idea one step further. As model problem, we consider once more the diffusion equation (2.1) and in addition a general convection-diffusion-reaction equation. In particular, the forthcoming construction of V_h will improve the stability of the discretization method for convection-dominated problems both when compared to a standard FEM and to previous BEM-based FEM approaches. The experiments also show an improved resolution of exponential layers at the outflow boundaries when the proposed method is compared to the Streamline Upwind/Petrov-Galerkin (SUPG) method [48].

6.2.1 Generalization for Diffusion Problem

In a first step we consider the generalization to polyhedral elements with polygonal faces for the diffusion problem (2.1). This problem reads

$$\begin{aligned} -\operatorname{div}(a\nabla u) &= f && \text{in } \Omega\ , \\ u &= g_D && \text{on } \Gamma_D\ , \\ a\nabla u \cdot \mathbf{n} &= g_N && \text{on } \Gamma_N\ , \end{aligned}$$

with the assumptions on the data as described in Chap. 2. Section 2.3 gives a detailed construction of basis functions for the two-dimensional case and a simple generalization for the three-dimensional case under the restriction that the polyhedral elements only have triangular faces. These functions are not limited to the diffusion equation, but they have been especially designed for that problem. Here, we first examine the situation for the first order approximation space V_h and give an alternative construction of its basis functions allowing polytopal elements with polygonal faces directly. Afterwards, we present the general space V_h^k yielding k-th order approximations.

If we look again into the two-dimensional case and the definition of the nodal basis functions (2.6), we observe that the values of the basis functions are fixed in the nodes and extended uniquely along the edges by linear functions. This linear extension is nothing else than a harmonic extension along the edge, and thus the

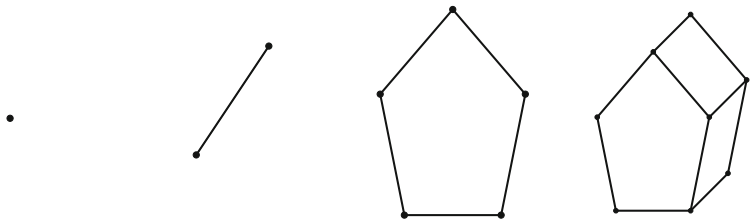

Fig. 6.6 Stepwise construction of basis functions

basis functions are also defined on the edges according to the underlying differential equation. Therefore, we propose a stepwise and hierarchical construction for the basis functions in the case of polyhedral elements with polygonal faces as sketched in Fig. 6.6. This approach has been first proposed in [147]. A similar idea has been used in two-dimensions for the construction of multiscale finite elements in [104].

In order to get a nodal basis of V_h, we declare for each node $\mathbf{z} \in \mathcal{N}_h$ a basis function $\psi_{\mathbf{z}}$ which is equal to one in $\mathbf{z}$ and zero in all other nodes of the mesh. Denoting the i-dimensional Laplace operator by Δ_i, we define the basis function $\psi_{\mathbf{z}}$ as unique solution of

$$
\begin{aligned}
-\Delta_3 \psi_{\mathbf{z}} &= 0 \quad \text{in } K \quad \text{for all } K \in \mathcal{K}_h \,, \\
-\Delta_2 \psi_{\mathbf{z}} &= 0 \quad \text{in } F \quad \text{for all } F \in \mathcal{F}_h \,, \\
-\Delta_1 \psi_{\mathbf{z}} &= 0 \quad \text{in } E \quad \text{for all } E \in \mathcal{E}_h \,, \\
\psi_{\mathbf{z}}(\mathbf{x}) &= \begin{cases} 1 & \text{for } \mathbf{x} = \mathbf{z} \,, \\ 0 & \text{for } \mathbf{x} \in \mathcal{N}_h \setminus \{\mathbf{z}\} \,, \end{cases}
\end{aligned}
$$

where the Laplace operators have to be understood in the corresponding linear parameter spaces. The values in the nodes are prescribed. Afterwards, we solve a Dirichlet problem for the Laplace equation on each edge. Then, we use the computed data as Dirichlet datum for the Laplace problem on each face, and finally, we proceed with the Laplace problem on each element, where the solutions on the faces are used as boundary values. In the case of convex faces and elements, these problems are understood in the classical sense and we have $\psi_{\mathbf{z}} \in C^2(K) \cap C^0(\overline{K})$. In the more general situation of non-convex elements, the weak solution is considered such that we have at least $\psi_{\mathbf{z}} \in H^1(K)$.

Building the span of these nodal basis functions, we obtain a first order approximation space $V_h = V_h^1$ on general meshes containing polyhedral elements with polygonal faces. In [147], this space has been analysed for its approximation properties and an interpolation operator analog to the one defined in Sect. 2.4 has been studied. The discrete Galerkin formulation for the model problem (2.1)

with the generalized approximation space applicable on polyhedral elements with polygonal faces reads as in Sect. 2.5, see (2.28).

Having this hierarchical construction in mind for the definition of nodal basis functions it is clear how to proceed with higher order basis functions. In the two-dimensional setting we enriched the approximation space with element bubble functions which have a polynomial Laplacian, see the motivation in Sect. 2.3.2. Thus, instead of prescribing the Laplace equation on edges, faces and elements, we use the Poisson equation with polynomial right hand side. Consequently, the discrete space V_h^k consists of function that are polynomials along the edges, their restriction onto a face $F \in \mathscr{F}_h$ lies in the two-dimensional approximation space $V_h^k(F)$ defined in Sect. 2.3.3, and they have a polynomial Laplacian inside the three-dimensional element $K \in \mathscr{K}_h$. More precisely, it is

$$V_h^k = \left\{ v \in H^1(\Omega) : \Delta v\big|_K \in \mathscr{P}^{k-2}(K) \; \forall K \in \mathscr{K}_h \text{ and } v\big|_F \in V_h^k(F) \; \forall F \in \mathscr{F}_h \right\} .$$

We easily see that $\mathscr{P}^k(K) \subset V_h^k\big|_K$, such that polynomials are contained in the approximation space locally. This ensures the approximation properties of the discrete space.

Remark 6.5 If the polyhedral elements have by chance only triangular faces, the approximation space described above is equivalent to the simple generalization from Sect. 2.3.4 for $k = 1$. In the case $k > 1$, however, the defined spaces differ between each other. On each triangular face F it is $\mathscr{P}^k(F) \subsetneq V_h^k(F)$ and whereas the simple generalization thus has $\frac{1}{2}(k-1)(k-2)$ internal degrees of freedom per face the above generalization has $\frac{1}{2}k(k-1)$.

6.2.2 Application to Convection-Diffusion-Reaction Problem

The general convection-diffusion-reaction problem in a bounded Lipschitz domain $\Omega \subset \mathbb{R}^3$ is given by

$$\begin{aligned} \mathrm{L}\, u = -\operatorname{div}(A\nabla u) + \mathbf{b} \cdot \nabla u + cu = 0 \quad & \text{in } \Omega \,, \\ u = g_D \quad & \text{on } \Gamma \,, \end{aligned} \tag{6.26}$$

where we restrict ourselves to the pure Dirichlet problem for shorter notation. Here $A(\mathbf{x}) \in \mathbb{R}^{3\times 3}$, $\mathbf{b}(\mathbf{x}) \in \mathbb{R}^3$, and $c(\mathbf{x}) \in \mathbb{R}$ are the coefficient functions of the partial differential operator L, and $g_D \in H^{1/2}(\Gamma)$ is the given Dirichlet data. We assume that $A(\cdot)$ is symmetric and uniformly positive with minimal eigenvalue $a_{\min}$, and that $c(\cdot)$ is non-negative. The corresponding Galerkin formulation reads as follows:

$$\begin{aligned} &\text{Find } u \in g_D + H_0^1(\Omega) : \\ &\int_\Omega (A\nabla u \cdot \nabla v + \mathbf{b} \cdot \nabla u \, v + cuv) \, \mathrm{d}\mathbf{x} = 0 \qquad \forall\, v \in H_0^1(\Omega) \,. \end{aligned} \tag{6.27}$$

We require that the coefficients A, $\mathbf{b}$, c are $L^\infty(\Omega)$, and that there exists a unique solution of (6.27). The unique solvability can be ensured under several well known conditions. For example, if $c - \frac{1}{2}\operatorname{div}(\mathbf{b}) \geq 0$, the bilinear form in (6.27) is $H_0^1(\Omega)$-elliptic, which guarantees the existence of a unique solution for the Dirichlet problem. Another sufficient condition is $a_{\min} c > |\mathbf{b}|^2$, see, e.g. [151]. Unique solvability of the variational problem (6.27) can be shown under quite general assumptions using results by Droniou [68].

For the application of the BEM-based FEM, we require that the coefficients $A(\cdot)$, $\mathbf{b}(\cdot)$, and $c(\cdot)$ are piecewise constant with respect to all geometrical objects in the polyhedral mesh $\mathscr{K}_h$. Since this is not the case in general, the coefficients are approximated by piecewise constant ones over the edges, faces and elements of the mesh. If the coefficients are smooth, we take their values in the center of mass of the geometrical objects as constant approximations. This corresponds to a first order approximation of the differential equation. If the coefficients are already piecewise constant with respect to the elements, we obtain their values on the edges and faces by computing averages over neighbouring elements. To simplify notation, we omit new symbols for this approximation. The resulting Dirichlet problem is uniquely solvable according to the before mentioned conditions in [68].

We restrict ourselves to the introduction of the first order approximation space. If the polyhedral elements consists of triangular faces only, we can proceed as for the simple generalization in Sect. 2.3.4. Consequently, the basis functions ψ are defined to be piecewise linear and continuous over the surface triangulation and satisfy the underlying differential equation inside each element, i.e., $\mathrm{L}\,\psi = 0$ in K, $\forall K \in \mathscr{K}_h$. This strategy has been introduced in [96] for the convection-diffusion-reaction equation. We refer to it as the original approach. There is a close relation between this original BEM-based FEM with piecewise linear boundary data and the so-called method of residual-free bubbles [41, 44, 45, 47, 80]. Indeed, it has been shown in [94] that the BEM-based FEM, with exact evaluation of the Steklov–Poincaré operator, is equivalent to the method of residual-free bubbles with exactly computed bubbles. Since the latter has been shown to be a stable method for convection-dominated problems, it seems clear that also the BEM-based FEM should have advantageous stability properties. It should be noted that neither the Steklov–Poincaré operator nor the computation of the residual-free bubbles can be realized exactly in practice.

In this chapter we follow the idea of the previous Sect. 6.2.1 and define the basis functions in a hierarchical fashion as in [99]. Thus, we obtain for each node $\mathbf{z} \in \mathscr{N}_h$ a basis function $\psi_{\mathbf{z}}$ as unique solution of

$$\begin{aligned}
\mathrm{L}\,\psi_{\mathbf{z}} &= 0 \quad \text{in } K \quad \text{for all } K \in \mathscr{K}_h\,, \\
\mathrm{L}_F\,\psi_{\mathbf{z}} &= 0 \quad \text{in } F \quad \text{for all } F \in \mathscr{F}_h\,, \\
\mathrm{L}_E\,\psi_{\mathbf{z}} &= 0 \quad \text{in } E \quad \text{for all } E \in \mathscr{E}_h\,,
\end{aligned}$$

$$\psi_{\mathbf{z}}(\mathbf{x}) = \begin{cases} 1 & \text{for } \mathbf{x} = \mathbf{z}\,, \\ 0 & \text{for } \mathbf{x} \in \mathscr{N}_h \setminus \{\mathbf{z}\}\,. \end{cases}$$

The differential operators L_E and L_F are projections of the differential operator L onto the edge E and the face F, respectively, see below for a precise description. Thus, the functions $\psi_{\mathbf{z}}$ are defined implicitly as local solutions of boundary value problems on edges, faces and elements of the decomposition. Equivalently, one can say that these functions are defined via PDE-harmonic extensions. The nodal data is first extended L_E-harmonically along the edges and afterwards, the data on the edges is extended into the faces with the help of a L_F-harmonic operator and so on.

For the definition of L_E and L_F, let $F \in \mathscr{F}_h$ be a face and $E \in \mathscr{E}_h$ an edge on the boundary of F. By rotation and translation of the coordinate system, we map the face F into the (e_1, e_2)-plane and the edge E onto the e_1-axis of the Euclidean coordinate system (e_1, e_2, e_3) such that one node of E lies in the origin. Thus, we have an orthogonal matrix $B \in \mathbb{R}^{3\times 3}$ and a vector $\mathbf{d} \in \mathbb{R}^3$ such that

$$\mathbf{x} \mapsto \widehat{\mathbf{x}} = B\mathbf{x} + \mathbf{d} \quad \text{and} \quad \widehat{\psi}(\widehat{\mathbf{x}}) = \psi(B^{-1}\widehat{\mathbf{x}} - B^{-1}\mathbf{d}) \,,$$

and the differential equation in (6.26) yields

$$-\operatorname{div}(A\nabla\psi)+\mathbf{b}\cdot\nabla\psi+c\psi = -\operatorname{div}_{\widehat{\mathbf{x}}}(BAB^\top\nabla_{\widehat{\mathbf{x}}}\widehat{\psi})+B\mathbf{b}\cdot\nabla_{\widehat{\mathbf{x}}}\widehat{\psi}+c\widehat{\psi} = 0 \,. \tag{6.28}$$

Here, the coefficients $BAB^\top$, $B\mathbf{b}$ and c are constant on F and E, respectively, since A, $\mathbf{b}$ and c are constant approximations on each geometrical object of the original coefficients. Furthermore, we only consider tangential components to define the operators L_F and L_E on the face and edge, respectively. This is equivalent to setting

$$\frac{\partial\widehat{\psi}}{\partial\widehat{x}_3} = \frac{\partial^2\widehat{\psi}}{\partial\widehat{x}_3^2} = 0 \text{ in } F \quad \text{and} \quad \frac{\partial\widehat{\psi}}{\partial\widehat{x}_2} = \frac{\partial\widehat{\psi}}{\partial\widehat{x}_3} = \frac{\partial^2\widehat{\psi}}{\partial\widehat{x}_2^2} = \frac{\partial^2\widehat{\psi}}{\partial\widehat{x}_3^2} = 0 \text{ on } E$$

in (6.28). Therefore, the dependence in (6.28) reduces to two and one coordinate directions such that L_F and L_E are defined as differential operators in two- and one-dimensions using the described coordinate system. Overall, the basis functions are constructed with the help of the convection-diffusion-reaction equation on the edges, faces and elements, where the diffusion matrix and the convection vector are adjusted in a proper way. All appearing one-, two- and three-dimensional boundary value problems are uniquely solvable due to the global properties of $A(\cdot)$, which carry over to $BAB^\top$, and since $c - \frac{1}{2}\operatorname{div}(B\mathbf{b}) = c \geq 0$ on F and E, respectively.

To simplify notation, we omit the coordinate transformation in the following and abbreviate the transformed diffusion matrix $BAB^\top$, the convection vector $B\mathbf{b}$ and the reaction term c to A_F, $\mathbf{b}_F$, c_F and A_E, $\mathbf{b}_E$, c_E on the faces and edges, respectively. Furthermore, we treat the basis functions $\psi_{\mathbf{z}}$ as functions of two or one variable depending on the underlying domain F or E. For example, let us assume that E already lies in the e_1-axis and corresponds to the interval $(0, h_E)$. In this case, $\psi_{\mathbf{z}}$ only depends on x_1 and the scalar valued coefficients A_E, $\mathbf{b}_E$, and c_E along E

and the differential equation reads

$$A_E \psi_{\mathbf{z}}'' + \mathbf{b}_E \psi_{\mathbf{z}}' + c_E \psi_{\mathbf{z}} = 0 \quad \text{in } (0, h_E) \,, \tag{6.29}$$

with some boundary data $\psi_{\mathbf{z}}(0)$ and $\psi_{\mathbf{z}}(h_E)$ that is 0 or 1 depending on the considered basis function.

Having the basis functions $\psi_{\mathbf{z}}$ at hand, we define the approximation spaces as

$$V_h = \operatorname{span}\{\psi_{\mathbf{z}} : \mathbf{z} \in \mathcal{N}_h\} \quad \text{and} \quad V_{h,D} = V_h \cap H_0^1(\Omega) \,. \tag{6.30}$$

The discrete Galerkin formulation thus reads:

$$\begin{aligned} &\text{Find } u_h \in g_D + V_{h,D} \subset V_h : \\ &\int_\Omega (A \nabla u_h \cdot \nabla v_h + \mathbf{b} \cdot \nabla u_h \, v_h + c u_h v_h) \, \mathrm{d}\mathbf{x} = 0 \qquad \forall \, v \in V_{h,D} \,. \end{aligned} \tag{6.31}$$

Remark 6.6 In order to define a high-order approximation space V_h^k with $k > 1$, we may proceed as in the previous Sect. 6.2.1. Consequently, additional edge, face and element bubble functions are introduced which are defined to satisfy the inhomogeneous convection-diffusion-reaction equation with polynomial right hand side inside the edges, faces and elements, respectively.

6.2.3 Realization of the Basis Functions

Of course, the hierarchically defined basis functions do not have a closed analytical form and they have to be treated numerically. In the following, we discuss this issue in more detail, where we solve the boundary value problems on the edges analytically, the problems on the faces with the help of a 2D FEM and the problems on the elements by means of boundary integral equations. For this purpose, an auxiliary discretization of the boundaries of the elements is needed. We apply the construction of the triangular surface mesh discussed in Sect. 2.2.2, which yields a conforming boundary discretization $\mathcal{T}_l(\partial K)$ of level l. Here, first the faces are discretized by connecting their vertices with the point $\mathbf{z}_F$ and afterwards, the resulting triangles are refined successively by splitting them into four similar triangles. According to this construction, the triangulations on all faces can be glued in a conforming manner to obtain a discretization of the whole boundary ∂K. In particular, the strategy yields for $l \geq 1$ a discretization of each edge in the mesh into line segments, see Fig. 6.7.

The advantage of this line of action is, that the two-dimensional finite element spaces on the faces of the elements fit exactly the approximation spaces utilized in three-dimensional boundary element methods. Thus, a 2D FEM approximation on the faces can directly be used in existing boundary element codes. Alternatively,

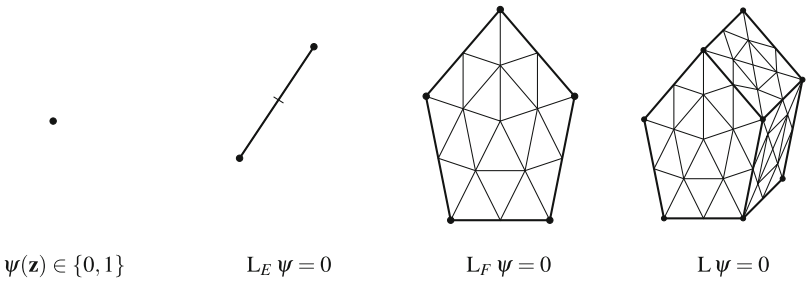

Fig. 6.7 Stepwise approximation of basis functions using the auxiliary discretization with $l = 1$

one might treat the boundary value problems on the faces by a 2D BEM in order to avoid the surface triangulation, but this would result in the need of a 3D BEM on polygonal surface meshes. Hence, we stick with the 2D FEM and 3D BEM strategy that is explained in more detail in the following. Furthermore, we restrict ourselves to $k = 1$.

To be mathematically more precise, we choose a basis function $\psi_{\mathbf{z}}$ and consider its approximation $\psi_{\mathbf{z},l}$ on the edges and faces of $K \in \mathscr{K}_h$ with $\mathbf{z} \in \mathscr{N}(K)$. Here, l refers to the level of the surface triangulation and therefore to the mesh size of the auxiliary discretization. We seek the approximation of $\psi_{\mathbf{z}}\big|_{\partial K}$, namely the Dirichlet data for the three-dimensional problem on K, as

$$g_{l,\partial K}^{(\psi_{\mathbf{z}})} \in \mathscr{P}^1_{\mathrm{pw}}(\mathscr{T}_l(\partial K)) \,, \quad \text{and set} \quad \psi_{\mathbf{z},l}\big|_{\partial K} = g_{l,\partial K}^{(\psi_{\mathbf{z}})} \,.$$

The space of piecewise linear polynomials over $\mathscr{T}_l(\partial K)$ has been endowed with a basis Φ_D in Sect. 4.3. We denote by $\underline{g}_{l,\partial K}^{(\psi_{\mathbf{z}})}$ the vector with the expansion coefficients of $g_{l,\partial K}^{(\psi_{\mathbf{z}})}$ in this basis. On all edges $E \in \mathscr{E}(K)$ with $\mathbf{z} \notin \mathscr{N}(E)$ and on all faces $F \in \mathscr{F}(K)$ with $\mathbf{z} \notin \mathscr{N}(F)$, the function $\psi_{\mathbf{z}}$ vanishes and it remains to consider the edges and faces with $\mathbf{z} \in \mathscr{N}(E)$ and $\mathbf{z} \in \mathscr{N}(F)$, respectively.

On Edges

For the pure diffusion problem, the basis functions are obviously linear along the edges with prescribed data in the nodes, which is either zero or one. In the convection-diffusion-reaction regime, however, L_E describes an ordinary differential operator of second order with constant and scalar-valued coefficients, cf. (6.29). Thus the boundary value problems on the edges are solved analytically and $\psi_{\mathbf{z}}$ can be written in closed form on each edge $E \in \mathscr{E}_h$. If $c_E = 0$, for instance, a small exercise shows

$$\psi_{\mathbf{z}}(x_1) = \psi_{\mathbf{z}}(0) + \big(\psi_{\mathbf{z}}(h_E) - \psi_{\mathbf{z}}(0)\big)\frac{1 - \exp\left(\frac{\mathbf{b}_E}{A_E} h_E x_1\right)}{1 - \exp\left(\frac{\mathbf{b}_E}{A_E} h_E\right)} \quad \text{for } x_1 \in [0, h_E] \,. \tag{6.32}$$

Here, we recognize how the data in the nodes for $x_1 = 0$ and $x_1 = h_E$ enter the formula.

For the diffusion problem we can express the linear function $\psi_{\mathbf{z}}\big|_E$ exact in the trace space of $\mathscr{P}^1_{\mathrm{pw}}(\mathscr{T}_l(\partial K))$ on E. For the convection-diffusion-reaction problem, however, we make use of the induced discretization of E into line segments and we interpolate $\psi_{\mathbf{z}}\big|_E$, cf. (6.32), by $g_{l,E}^{(\psi_{\mathbf{z}})}$ in the space of piecewise linear functions over the discretization of E. Finally, the functions $g_{l,E}^{(\psi_{\mathbf{z}})}$ on the edges $E \in \mathscr{E}(F)$ are combined in order to obtain the Dirichlet data $g_{l,\partial F}^{(\psi_{\mathbf{z}})}$ on ∂F for the 2D problems on the faces of the element.

On Faces

The variational formulation for $\psi_{\mathbf{z}}\big|_F$ reads analog to (6.27). The non-homogeneous Dirichlet data is treated as usual in the Galerkin formulation. Therefore, we interpret $g_{l,\partial F}^{(\psi_{\mathbf{z}})}$ as extension into $\mathscr{P}^1_{\mathrm{pw}}(\mathscr{T}_l(F))$. Furthermore, we denote by $\Phi_{D,F}$ the set of basis functions from Φ_D with support in F, such that

$$\operatorname{span} \Phi_{D,F} = \mathscr{P}^1_{\mathrm{pw}}(\mathscr{T}_l(F)) \cap H^1_0(F) \,.$$

In the case of the pure diffusion problem, the discrete Galerkin formulation for the approximation of the basis functions on the faces $F \in \mathscr{F}(K)$ reads:

$$\text{Find } g_{l,F}^{(\psi_{\mathbf{z}})} \in g_{l,\partial F}^{(\psi_{\mathbf{z}})} + \operatorname{span} \Phi_{D,F} : \quad \int_F \nabla g_{l,F}^{(\psi_{\mathbf{z}})} \cdot \nabla \varphi \, \mathrm{d}s_{\mathbf{x}} = 0 \quad \forall \varphi \in \Phi_{D,F} \,.$$

We point out that the boundary data on the edges is linear in this case. Hence, it is represented exact in the space of piecewise polynomials. Furthermore, if the faces $F \in \mathscr{F}(K)$ are already triangles, we recover the basis functions discussed in the simple generalization to 3D in Sect. 2.3.4.

In the case of the convection-diffusion-reaction equation we might encounter convection-dominated problems. Consequently, we propose to utilize a stabilized FEM on the faces. We choose the Streamline Upwind/Petrov-Galerkin (SUPG) method [48] such that the discrete formulation for the approximation of the basis functions on the faces reads:

$$\begin{aligned} &\text{Find } g_{l,F}^{(\psi_{\mathbf{z}})} \in g_{l,\partial F}^{(\psi_{\mathbf{z}})} + \operatorname{span} \Phi_{D,F} : \\ &\int_F (A_F \nabla g_{l,F}^{(\psi_{\mathbf{z}})} \cdot \nabla \varphi + \mathbf{b}_F \cdot \nabla g_{l,F}^{(\psi_{\mathbf{z}})} \, \varphi + c_F g_{l,F}^{(\psi_{\mathbf{z}})} \, \varphi) \, \mathrm{d}s_{\mathbf{x}} \\ &\qquad + \delta_F \int_F (\mathbf{b}_F \cdot \nabla g_{l,F}^{(\psi_{\mathbf{z}})} \, \mathbf{b}_F \cdot \nabla \varphi + c_F g_{l,F}^{(\psi_{\mathbf{z}})} \, \mathbf{b}_F \cdot \nabla \varphi) \, \mathrm{d}s_{\mathbf{x}} = 0 \quad \forall \varphi \in \Phi_{D,F} \,, \end{aligned} \tag{6.33}$$

where $\delta_F \geq 0$ is a stabilization parameter which is set to zero in the diffusion-dominated case. The choice of δ_F is discussed in more detail in Sect. 6.2.6. On all faces $F \in \mathscr{F}_h$ with $\mathbf{z} \notin \mathscr{N}(F)$, it is $g_{l,F}^{(\psi_{\mathbf{z}})} = 0$. Here, we point out that the

boundary data on the edges is not polynomial in general, cf. (6.32). Thus, $g_{l,\partial F}^{(\psi_{\mathbf{z}})}$ is an approximation of the actual data.

Finally, the functions $g_{l,F}^{(\psi_{\mathbf{z}})}$ on the faces $F \in \mathscr{F}(K)$ are combined in order to obtain the Dirichlet data $g_{l,\partial K}^{(\psi_{\mathbf{z}})} \in \mathscr{P}^1_{\mathrm{pw}}(\mathscr{T}_l(\partial K))$ for the 3D problems on the whole boundary of the element. This construction is well defined since the triangulations of the faces form a conforming discretization of the surface ∂K, cf. Fig. 6.7.

On Elements

After we have computed the Dirichlet traces $g_l^{(\psi_{\mathbf{z}})}$ of all the approximate basis functions $\psi_{\mathbf{z},l}$ on the skeleton of the discretization, i.e., on the boundaries of the polyhedral elements, the three-dimensional local problems are treated by means of boundary integral equations and they are approximated by the boundary element method. For the pure diffusion problem we proceed as discussed in Chap. 4. Consequently, we have the Steklov–Poincaré operator (4.7), which maps the Dirichlet to the Neumann trace, and the representation formula (4.3) for the evaluation of the approximation inside the elements. The approximation of the Steklov–Poincaré operator and the representation formula are given in (4.20) and (4.22), respectively. In particular, the approximation space in the 2D FEM on the faces has been chosen in such a way that $g_{l,\partial K}^{(\psi_{\mathbf{z}})} \in \mathscr{P}^1_{\mathrm{pw}}(\mathscr{T}_l(\partial K))$ for $\psi_{\mathbf{z},l}$ with $\mathbf{z} \in \mathscr{N}(K)$ and $K \in \mathscr{K}_h$. Hence, we can apply directly the results of Sect. 4.3.

The boundary element method is not restricted to the Laplace equation. It generalizes to a large class of problems where the corresponding fundamental solutions are known. This is in particular true for the convection-diffusion-reaction equation. Here, the fundamental solution depends on A_K, $\mathbf{b}_K$ as well as on c_K and consequently on the element $K \in \mathscr{K}_h$. In $\mathbb{R}^3$ and under the assumption $c_K + \|\mathbf{b}_K\|^2_{A_K^{-1}} \geq 0$, we have

$$U_K^*(\mathbf{x},\mathbf{y}) = \frac{1}{4\pi\sqrt{\det A_K}} \frac{\exp\left(\mathbf{b}_K^\top A_K^{-1}(\mathbf{x}-\mathbf{y}) - \lambda\|\mathbf{x}-\mathbf{y}\|_{A_K^{-1}}\right)}{\|\mathbf{x}-\mathbf{y}\|_{A_K^{-1}}} \quad \text{for } \mathbf{x},\mathbf{y} \in \mathbb{R}^3 ,$$

where

$$\|\mathbf{x}\|_{A_K^{-1}} = \sqrt{\mathbf{x}^\top A_K^{-1}\mathbf{x}} \quad \text{and} \quad \lambda = \sqrt{c_K + \|\mathbf{b}_K\|^2_{A_K^{-1}}} .$$

With the help of $U_K^*(\cdot,\cdot)$, which satisfies

$$\mathrm{L}_{\mathbf{y}}\, U_K^*(\mathbf{x},\mathbf{y}) = \delta_0(\mathbf{y}-\mathbf{x})$$

for the convection-diffusion-reaction operator L, where δ_0 is the Dirac delta distribution, we can formulate the boundary integral operators as in Sect. 4.2. Since L is not a self-adjoint operator, we have to distinguish between the conormal

derivative $\gamma_1^K v$, which is given for sufficiently smooth v as

$$(\gamma_1^K v)(\mathbf{x}) = \mathbf{n}_K(\mathbf{x}) \cdot (\gamma_0^K A_K \nabla v)(\mathbf{x}) \quad \text{for } \mathbf{x} \in \partial K \ ,$$

and the modified conormal derivative

$$\widetilde{\gamma_1^K} v = \gamma_1^K v + (\mathbf{b}_K \cdot \mathbf{n}_K)\gamma_1^K v \ , \tag{6.34}$$

which is associated with the adjoint problem. The conormal derivative is also called Neumann trace. For $\mathbf{x} \in \partial K$, we have the single-layer potential operator

$$(\mathbf{V}_K \zeta)(\mathbf{x}) = \gamma_0^K \int_{\partial K} U_K^*(\mathbf{x}, \mathbf{y}) \zeta(\mathbf{y}) \, \mathrm{d}s_{\mathbf{y}} \quad \text{for } \zeta \in H^{-1/2}(\partial K) \ ,$$

the double-layer potential operator

$$(\mathbf{K}_K \xi)(\mathbf{x}) = \lim_{\varepsilon \to 0} \int\limits_{\mathbf{y} \in \partial K : |\mathbf{y} - \mathbf{x}| \geq \varepsilon} \widetilde{\gamma_{1,\mathbf{y}}^K} U_K^*(\mathbf{x}, \mathbf{y}) \xi(\mathbf{y}) \, \mathrm{d}s_{\mathbf{y}} \quad \text{for } \xi \in H^{1/2}(\partial K) \ ,$$

and the adjoint double-layer potential operator

$$(\mathbf{K}_K' \zeta)(\mathbf{x}) = \lim_{\varepsilon \to 0} \int\limits_{\mathbf{y} \in \partial K : |\mathbf{y} - \mathbf{x}| \geq \varepsilon} \gamma_{1,\mathbf{x}}^K U_K^*(\mathbf{x}, \mathbf{y}) \zeta(\mathbf{y}) \, \mathrm{d}s_{\mathbf{y}} \quad \text{for } \zeta \in H^{-1/2}(\partial K) \ ,$$

as well as the hypersingular integral operator

$$(\mathbf{D}_K \xi)(\mathbf{x}) = -\gamma_1^K \int_{\partial K} \widetilde{\gamma_{1,\mathbf{y}}^K} U_K^*(\mathbf{x}, \mathbf{y}) \xi(\mathbf{y}) \, \mathrm{d}s_{\mathbf{y}} \quad \text{for } \xi \in H^{1/2}(\partial K) \ .$$

These operators have the same mapping properties as the corresponding integral operators for the Laplace operator. We point out that they differ in the fundamental solution $U_K^*(\cdot, \cdot)$ and the use of the modified conormal derivative. As in Chap. 4, we have a representation formula and two representations of the Steklov–Poincaré operator, which maps the Dirichlet to the Neumann trace

$$\gamma_1^K u = \mathbf{S}_K \gamma_0^K u \ ,$$

in terms of the boundary integral operators:

$$\mathbf{S}_K = \mathbf{V}_K^{-1}(\tfrac{1}{2}\mathbf{I} + \mathbf{K}_K) = \mathbf{D}_K + (\tfrac{1}{2}\mathbf{I} + \mathbf{K}_K')\mathbf{V}_K^{-1}(\tfrac{1}{2}\mathbf{I} + \mathbf{K}_K) \ , \tag{6.35}$$

provided that $\mathbf{V}_K$ is invertible. The invertibility of the single-layer potential operator $\mathbf{V}_K$ is shown for some special cases, like the Laplace operator or when the material parameters satisfy $a_{\min} c_K > |\mathbf{b}_K|^2$, where $a_{\min}$ is the minimal eigenvalue of A_K,

see [151]. For general elliptic operators as in (6.26) with constant coefficients, Costabel [61] has shown that the single-layer potential is a strongly elliptic operator and thus satisfies a Gårding inequality. The discretization of these boundary integral operators follows the line of Sect. 4.3, where the boundary mesh $\mathscr{B}_h$ is chosen to be $\mathscr{T}_l(\partial K)$. Hence, we obtain the corresponding boundary element matrices $\mathbf{V}_{K,l}$, $\mathbf{M}_{K,l}$, $\mathbf{K}_{K,l}$ and so on.

6.2.4 Fully Discrete Galerkin Formulation

We consider the convection-diffusion-reaction equation only, since it includes the pure diffusion problem, and we restrict ourselves for shorter notation to Dirichlet boundary conditions and a vanishing source term as in (6.26). Instead of applying the approximation space (6.30) with the implicitly defined basis functions on edges, faces and elements, we use the spaces

$$V_{h,l} = \operatorname{span}\{\psi_{\mathbf{z},l} : \mathbf{z} \in \mathscr{N}_h\} \quad \text{and} \quad V_{h,l,D} = V_{h,l} \cap H_0^1(\Omega) \,,$$

which are spanned by the approximated basis function $\psi_{\mathbf{z},l}$ as described in the previous Sect. 6.2.3. This approximation space is conforming, i.e. $V_{h,l} \subset H^1(\Omega)$, due to the continuity of the functions in $V_{h,l}$ over edges as well as faces and because of the regularity of the local problems defining the basis functions. The discrete Galerkin formulation reads:

$$\text{Find } u_{h,l} \in g_D + V_{h,l,D} : \quad b(u_{h,l}, v_{h,l}) = 0 \quad \forall v_{h,l} \in V_{h,l,D} \,, \tag{6.36}$$

with bilinear form

$$b(u_{h,l}, v_{h,l}) = \int_\Omega \left(A \nabla u_{h,l} \cdot \nabla v_{h,l} + \mathbf{b} \cdot \nabla u_{h,l}\, v_{h,l} + c\, u_{h,l} v_{h,l} \right) \mathrm{d}\mathbf{x} \,.$$

For the realization of the bilinear form, we proceed as in Sect. 4.5. Integration by parts and the properties of $V_{h,l}$ yield

$$\begin{aligned} b(u_{h,l}, v_{h,l}) &= \sum_{K \in \mathscr{K}_h} \int_K \left(A_K \nabla u_{h,l} \cdot \nabla v_{h,l} + \mathbf{b}_K \cdot \nabla u_{h,l}\, v_{h,l} + c_K\, u_{h,l} v_{h,l} \right) \mathrm{d}\mathbf{x} \\ &= \sum_{K \in \mathscr{K}_h} \int_{\partial K} \gamma_1^K u_{h,l}\, \gamma_0^K v_{h,l}\, \mathrm{d}s_{\mathbf{x}} + \int_K \mathrm{L}\, u_{h,l}\, v_{h,l}\, \mathrm{d}\mathbf{x} \\ &= \sum_{K \in \mathscr{K}_h} \int_{\partial K} \mathbf{S}_K \gamma_0^K u_{h,l}\, \gamma_0^K v_{h,l}\, \mathrm{d}s_{\mathbf{x}} \,. \end{aligned}$$

Next, we replace the Steklov–Poincaré operator by its non-symmetric or symmetric representation, cf. (6.35), and approximate it by means of boundary element methods in analog to Sect. 4.5. Let $\underline{g}_{l,\partial K}^{(u)}$ and $\underline{g}_{l,\partial K}^{(v)}$ be the vectors with the expansion coefficients of $\gamma_0^K u_{h,l}$ and $\gamma_0^K v_{h,l}$ in $\mathscr{P}^1_{\mathrm{pw}}(\mathscr{T}_l(\partial K))$, respectively. These vectors are given as linear combinations of the coefficient vectors $\underline{g}_{l,\partial K}^{(\psi_{\mathbf{z}})}$ from the basis functions $\psi_{\mathbf{z}}$ computed in Sect. 6.2.3 on the faces. Consequently, we obtain for $b(\cdot,\cdot)$ the approximation

$$b_l(u_{h,l}, v_{h,l}) = \sum_{K \in \mathscr{K}_h} (\underline{g}_{l,\partial K}^{(v)})^\top S_{K,l}\, \underline{g}_{l,\partial K}^{(u)} \ ,$$

where $S_{K,l} \in \mathbb{R}^{|\mathscr{M}_l(\partial K)| \times |\mathscr{M}_l(\partial K)|}$ is either

$$\mathbf{S}_{K,l}^{\mathrm{unsym}} = \mathbf{M}_{K,l}^\top \mathbf{V}_{K,l}^{-1} \left(\tfrac{1}{2}\mathbf{M}_{K,l} + \mathbf{K}_{K,l} \right) \ ,$$

when using the non-symmetric representation, or

$$\mathbf{S}_{K,l} = \mathbf{D}_{K,l} + \left(\tfrac{1}{2}\mathbf{M}_{K,l}^\top + \mathbf{K}_{K,l}^\top \right) \mathbf{V}_{K,l}^{-1} \left(\tfrac{1}{2}\mathbf{M}_{K,l} + \mathbf{K}_{K,l} \right) ,$$

when using the symmetric representation of the Steklov–Poincaré operator. Here, the matrices in bold letters are the corresponding boundary element matrices for the convection-diffusion-reaction operator defined in Sect. 6.2.3. For this differential operator, however, the hypersingular integral operator $\mathbf{D}_K$ is not self-adjoint and hence, $\mathbf{D}_{K,l}$ is non-symmetric. Consequently, the symmetric representation of the Steklov–Poincaré operator yields a non-symmetric matrix $\mathbf{S}_{K,l}$.

Finally, the fully discrete Galerkin formulation reads:

$$\text{Find } u_{h,l} \in g_D + V_{h,l,D} : \quad b_l(u_{h,l}, v_{h,l}) = 0 \quad \forall v_{h,l} \in V_{h,l,D} \ . \tag{6.37}$$

The assembling of the global FEM matrix is performed as usual by adding up the local element-wise contributions. Therefore, let $D_K \in \mathbb{R}^{|\mathscr{M}_l(\partial K)| \times |\mathscr{N}(K)|}$ be the matrix obtained by gathering the vectors $\underline{g}_{l,\partial K}^{(\psi_{\mathbf{z}})} \in \mathbb{R}^{|\mathscr{M}_l(\partial K)|}$, $\mathbf{z} \in \mathscr{N}(K)$ with the expansion coefficients of $\gamma_0^K \psi_{\mathbf{z},l}$ in $\mathscr{P}^1_{\mathrm{pw}}(\mathscr{T}_l(\partial K))$ computed in Sect. 6.2.3. The matrix

$$D_K^\top S_{K,l} D_K \in \mathbb{R}^{|\mathscr{N}(K)| \times |\mathscr{N}(K)|}$$

with either $S_{K,l} = \mathbf{S}_{K,l}^{\mathrm{unsym}}$ or $S_{K,l} = \mathbf{S}_{K,l}$ serves as local stiffness matrix in the BEM-based FEM simulation. At this point we emphasize that the local auxiliary triangulations $\mathscr{T}_l(\partial K)$ are used only to compute the element stiffness matrices. The level of refinement l chosen for them has no influence on the size of the global FEM system.

6.2.5 Numerical Experiments: Diffusion Problem

In the setup of the local boundary element matrices, we use a semi analytical integration scheme. The inner integral in the Galerkin matrices is evaluated analytically and the outer one is approximated by Gaussian quadrature. For the assembling of the global FEM system matrix we use locally the stiffness matrices resulting from the non-symmetric representation of the Steklov–Poincaré operator, see Sect. 6.2.4. Since this formulation yields non-symmetric local stiffness matrices although the bilinear form is symmetric, we apply a symmetrization in order to retain the symmetry. We write

$$\begin{aligned} b(u_{h,l}, v_{h,l}) &= \sum_{K \in \mathscr{K}_h} \int_K a_K \nabla u_{h,l} \cdot \nabla v_{h,l} \mathrm{d}\mathbf{x} \\ &= \sum_{K \in \mathscr{K}_h} \frac{a_K}{2} \Big(\int_{\partial K} \gamma_1^K u_{h,l}\, \gamma_0^K v_{h,l}\, \mathrm{d}s_{\mathbf{x}} + \int_{\partial K} \gamma_1^K v_{h,l}\, \gamma_0^K u_{h,l}\, \mathrm{d}s_{\mathbf{x}} \Big) , \end{aligned}$$

and use the approximation

$$b_l(u_{h,l}, v_{h,l}) = \sum_{K \in \mathscr{K}_h} \frac{a_K}{2} (\underline{g}_{l,\partial K}^{(v)})^\top \left(\mathbf{S}_{K,l}^{\mathrm{unsym}} + (\mathbf{S}_{K,l}^{\mathrm{unsym}})^\top \right) \underline{g}_{l,\partial K}^{(u)} ,$$

which yields locally the symmetric stiffness matrix

$$\frac{a_K}{2} D_K^\top \left(\mathbf{S}_{K,l}^{\mathrm{unsym}} + (\mathbf{S}_{K,l}^{\mathrm{unsym}})^\top \right) D_K \in \mathbb{R}^{|\mathscr{N}(K)| \times |\mathscr{N}(K)|} .$$

The symmetric systems of linear equations arising on the faces and in the global FEM system are solved by the conjugate gradient method [90] without any preconditioning. Of course, for larger problems a more efficient solver is of particular interest. It is possible to use FETI-type strategies, for instance. The application of such solvers to the BEM-based FEM has been studied in [94, 97].

The first numerical example in this section is formulated on the unit cube. We utilize Voronoi meshes which are a particular example of polyhedral meshes. In Fig. 6.8, the first three meshes of the sequence are visualized which are used for the convergence experiments. We see that the elements are non-trivial polyhedra with arbitrary polygonal faces. The meshes have been produced by generating random points according to [71] and constructing the corresponding Voronoi diagram in accordance with [70]. It is assumed that the mesh generator provides the points $\mathbf{z}_K$ and $\mathbf{z}_F$ from the Definitions 2.10 and 2.11. However, for convex elements and faces we may use the center of mass instead which is computable.

In Table 6.1, we sketch the number of elements $|\mathscr{K}_h|$ and the number of nodes $|\mathscr{N}_h|$ in the different Voronoi meshes. The proposed strategy approximates the solution by a linear combination of as many basis function as nodes are in

Fig. 6.8 Sequence of Voronoi meshes

Table 6.1 Total number of nodes and elements when working with triangulated surfaces of different mesh levels l

$\lvert\mathscr{K}_h\rvert$	$\lvert\mathscr{N}_h\rvert$	$l=0$	$l=1$	$l=2$
9	46	98	424	1790
76	416	905	4170	18,011
712	4186	9081	42,446	184,170
1316	7850	17,013	79,676	345,903
5606	34,427	74,457	349,663	1,519,143
26,362	164,915	356,189	1,675,171	7,280,603

the mesh. Therefore, the number of degrees of freedom in the BEM-based FEM is $|\mathscr{N}_h|$ minus the number of nodes on the Dirichlet boundary Γ_D. The simple generalization for the first order method from Sect. 2.3.4, initially proposed in [60], needs to triangulate the surfaces of the elements and the number of basis functions corresponds to the total number of nodes after the triangulation. In Table 6.1, this total number of nodes is listed in the case that the faces are triangulated with the level $l = 0, 1, 2$, cf. Fig. 6.9. We recognize that in this situation much more basis functions and thus degrees of freedom are required in the global computations. Roughly speaking, the number of nodes doubles if the coarsest discretization of the faces is used. If a finer triangulation is needed, the number of nodes and thus the number of degrees of freedom increase 10 times for $l = 1$ and even more than forty times for $l = 2$. Since the diameter of the elements are equal in all four situations, the approximation errors of the finite element computations are of the same order for fixed l. However, the constant in [60] might be better than the one obtained for the presented strategy for vanishing right hand side in the differential equation. This is due to the fact that if h is fixed and only l is increased, the method in [60] still converges since it is equivalent to a boundary element domain decomposition approach [106]. The hierarchical construction proposed in this chapter gives for small l comparable approximations while requiring a minimal set of degrees of freedoms.

In the following, we investigate the influence of the face discretization. These triangulations of the faces are utilized to define the approximated basis functions

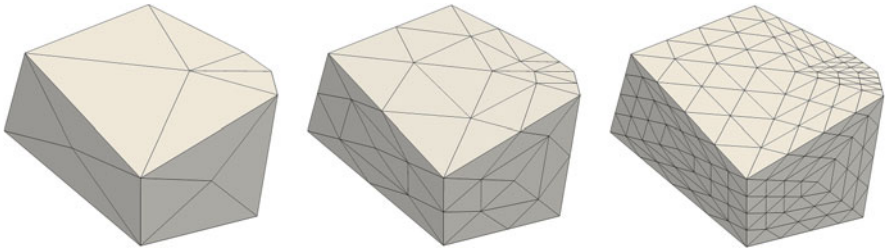

Fig. 6.9 Polyhedral element with surface triangulations of level $l = 0, 1, 2$

Table 6.2 Number of nodes $|\mathscr{M}_l(\partial K)|$ and number of triangles $|\mathscr{T}_l(\partial K)|$ in the surface discretization of the element in Fig. 6.9 for different levels

$\lvert\mathscr{N}(K)\rvert$	l	$\lvert\mathscr{M}_l(\partial K)\rvert$	$\lvert\mathscr{T}_l(\partial K)\rvert$
12	0	20	36
	1	74	144
	2	290	576
	3	1154	2304
	4	4610	9216

$\psi_{\mathbf{z},l}$ on the faces with the help of local, two-dimensional finite element methods. The finer the discretization is chosen the better we approximate the original basis functions $\psi_{\mathbf{z}}$. Even though, the face discretization does not blow up the global system matrix, the computational effort for the local problems increases if the discretization level l is raised. As one example, we pick the element K from Fig. 6.9 and list the number of nodes $|\mathscr{M}_l(\partial K)|$ and the number of triangles $|\mathscr{T}_l(\partial K)|$ in the surface discretization of K for different levels l in Table 6.2. The main tasks in the local problems are the evaluation of the boundary element matrix entries and the inversion of the single-layer potential matrix $\mathbf{V}_{K,l}$, which gives a local complexity of $\mathscr{O}(|\mathscr{T}_l(\partial K)|^3)$.

Next, the rates of convergence are analysed for different values of l. Therefore, consider the Dirichlet boundary value problem

$$-\Delta u = 0 \quad \text{in } \Omega = (0,1)^3\,, \qquad u = g_D \quad \text{on } \Gamma\,,$$

on the sequence of Voronoi meshes, where g_D is chosen such that

$$u(\mathbf{x}) = \exp(2\sqrt{2}\pi(x_1 - 0.3))\cos(2\pi(x_2 - 0.3))\sin(2\pi(x_3 - 0.3)) \tag{6.38}$$

is the exact solution. The relative errors in the energy and L_2-norm, i.e.

$$\frac{\|u - u_{h,l}\|_b}{\|u\|_b} \qquad \text{and} \qquad \frac{\|u - u_{h,l}\|_{L_2(\Omega)}}{\|u\|_{L_2(\Omega)}}\,,$$

are given in Fig. 6.10 with respect to $h = \max\{h_K : K \in \mathscr{K}_h\}$ in logarithmic scale for different discretization levels $l = 0, 1, 2$. This example shows that

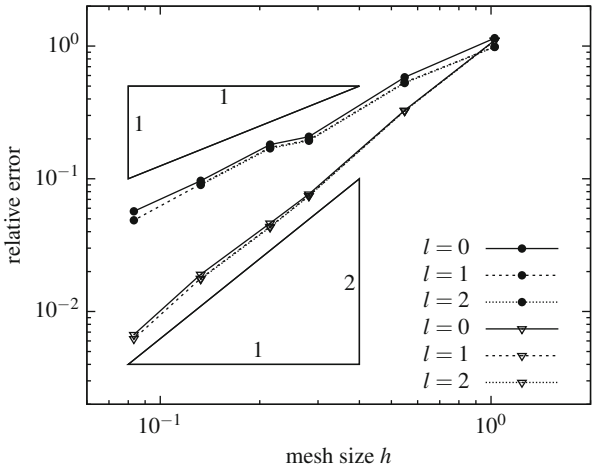

Fig. 6.10 Relative error in $\|\cdot\|_b$ (•) and $\|\cdot\|_{L_2(\Omega)}$ (▽) with respect to h for levels $l = 0, 1, 2$ in the example with solution (6.38)

the discretization level of the faces does not influence the rates of convergence as proofed in [147]. Additionally, Fig. 6.10 indicates that the constant in the error estimate can be chosen to be independent of the level l. The coarsest face discretization with $l = 0$ is sufficient to analyse the convergence rates in the forthcoming numerical experiments. Due to this choice, the local complexity in the two-dimensional finite element method on the faces $F \in \mathscr{F}_h$ and the local boundary element methods on the elements $K \in \mathscr{K}_h$ is rather small. Furthermore, in Fig. 6.10, we recognize linear convergence for the approximation error measured in the energy norm and quadratic convergence if the error is measured in the L_2-norm as expected, see [147].

Finally, we consider the model problem on a L-shaped domain with a singular solution such that $u \notin H^2(\Omega)$, but $u \in H^{5/3}(\Omega)$. Due to the theory of interpolation spaces, see, e.g., [34], we expect a convergence order of $2/3$. With the help of cylindrical coordinates (r, ϕ, x_3), where $r \geq 0$, $\phi \in [\pi/2, 2\pi]$ and $x_3 \in \mathbb{R}$, the function

$$u(r\cos\phi, r\sin\phi, x_3) = r^{2/3}\sin(\tfrac{2}{3}(\phi - \tfrac{\pi}{2})) \in H^{5/3}(\Omega) \tag{6.39}$$

satisfies the Laplace equation in the L-shaped domain

$$\Omega = \big((-1,1)\times(-1,1)\times(0,1)\big) \setminus [0,1]^3$$

with appropriate Dirichlet data. The boundary value problem is solved by means of the BEM-based FEM on a sequence of polyhedral meshes made of polygonal bricks, i.e., the meshes contain as elements prisms having general polygonal ends. In Fig. 6.11, we give the initial mesh of the domain Ω with hanging nodes and

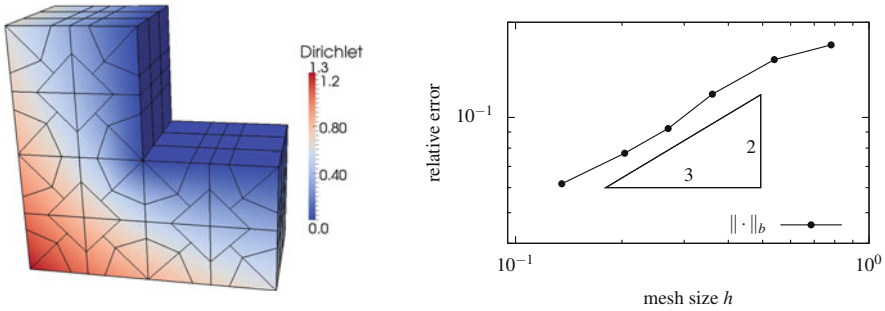

Fig. 6.11 L-shaped domain with polyhedral mesh made of bricks and Dirichlet data (left) and relative error $\|u - u_{h,l}\|_b / \|u\|_b$ with respect to h for $l = 0$ in the example with solution (6.39) (right)

edges. Additionally, we show the relative error $\|u - u_{h,l}\|_b / \|u\|_b$ with respect to $h = \max\{h_K : K \in \mathscr{K}_h\}$ in logarithmic scale. As expected, we obtain the reduced order of convergence for a sequence of uniform refined meshes. To recover the linear convergence in the energy norm for singular solutions, it is necessary to perform adaptive mesh refinement strategies as discussed in Chap. 5.

6.2.6 *Numerical Experiments: Convection-Diffusion Problem*

In this section, we give some implementation details as well as numerical experiments for the convection-diffusion problem. The computations are done on tetrahedral and polyhedral meshes. For the sake of simplicity, we restrict ourselves to the case of scalar valued diffusion coefficients, i.e., $A = \alpha I$ for some $\alpha > 0$, and a vanishing reaction term $c = 0$. Furthermore, the experiments are carried out with constant and continuously varying convection vector $\mathbf{b}$. Remember, that we have to approximate the coefficients α and $\mathbf{b}$ by constants on each geometrical object for the BEM-based FEM, see Sect. 6.2.2. The method is studied for the case of decreasing diffusion $\alpha \to 0$. Standard numerical schemes like the finite element method become unstable when applied to this type of convection-dominated problems. Typically, the issue manifests itself in the form of spurious oscillations. The critical quantity here is the mesh Péclet number

$$\mathrm{Pe}_K = \frac{h_K |\mathbf{b}_K|}{\alpha_K}, \quad K \in \mathscr{K}_h ,$$

which should be bounded by 2 for standard finite element methods. In the numerical experiments, we give $\mathrm{Pe}_h = \max\{\mathrm{Pe}_K : K \in \mathscr{K}_h\}$. When decreasing the diffusion for fixed h, the mesh Péclet number increases and we expect oscillations. This is

due to the fact that the boundary value problem gets closer to a transport equation and thus, boundary layers appear near the outflow boundary.

In addition to stability, we study the number of GMRES iterations, which are used to compute the approximate solution of the resulting system of linear equations, and we compare the presented approach with a 3D SUPG implementation.

Implementation Details

All computations regarding the convection-adapted basis functions can be done in a preprocessing step. In the case of non-constant convection, diffusion and reaction, these terms are first projected into the space of piecewise constant functions over the edges, faces and elements of the mesh. Afterwards, the Dirichlet traces of the basis functions are computed on the edges and faces. Here, an analytic formula is utilized on each edge $E \in \mathscr{E}_h$, and subsequently, the two-dimensional convection-diffusion-reaction problems are treated separately on each face $F \in \mathscr{F}_h$ according to the SUPG formulation (6.33). Let the local Péclet number be defined by

$$\mathrm{Pe}_{F,T} = \frac{h_T |\mathbf{b}_F|}{\alpha_F} \quad \text{for } T \in \mathscr{T}_l(F) \ .$$

The stabilization parameter δ_F in the SUPG method is chosen to be piecewise constant over the auxiliary triangulation $\mathscr{T}_l(F)$ on each face $F \in \mathscr{F}_h$. The choice

$$\delta_{F,T} = \begin{cases} c_1 h_T/2 & \text{for } \mathrm{Pe}_{F,T} > 2 \ , \\ c_2 h_T^2/\alpha_F & \text{else} \ , \end{cases}$$

leads to the best possible convergence rate of the discrete solution with respect to the streamline diffusion norm on F, see [149]. However, an 'optimal' choice of the constants c_1 and c_2 is not known. Since we aim to omit additional user defined parameters, the choice

$$\delta_{F,T} = \frac{h_T}{2|\mathbf{b}_F|} \left(\frac{1}{\tan(\mathrm{Pe}_{F,T})} - \frac{1}{\mathrm{Pe}_{F,T}} \right) \ , \tag{6.40}$$

is preferred in the numerical realization, see [111].

The auxiliary triangulations $\mathscr{T}_l(F)$ of level $l \in \mathbb{N}_0$ are constructed as described in Sect. 2.2 and visualized in Figs. 2.4 and 6.9, for example. But, in case of convection-dominated problems on the faces, we decided to move the midpoint $\mathbf{z}_F$ of the mesh, created in $\mathscr{T}_0(F)$, into the direction of the projected convection vector $\mathbf{b}_F$, see Fig. 6.12 (middle). If $\kappa > 0$ is such that $\mathbf{z}_F + \kappa \mathbf{b}_F \in \partial F$, then the translation can be chosen as

$$\mathbf{z}_F \mapsto \mathbf{z}_F + (1 - \vartheta)\kappa \mathbf{b}_F \ , \quad \text{with transition point} \quad \vartheta = \min \left\{ \frac{1}{2}, \frac{\alpha_F}{|\mathbf{b}_F|} \log(l+1) \right\} .$$

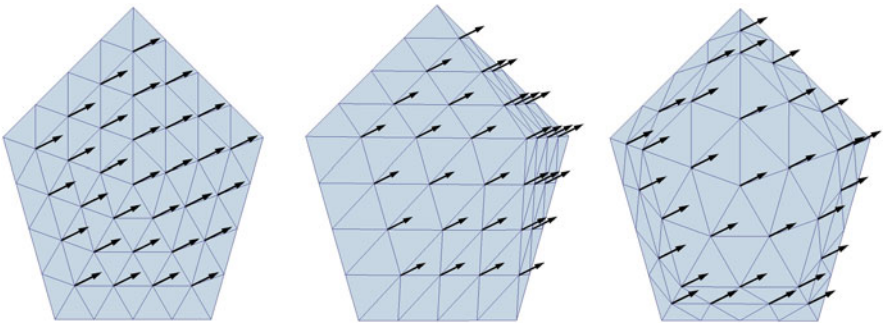

Fig. 6.12 Adaptation of auxiliary triangulation $\mathscr{T}_2(F)$ and projected convection vector: without adaptation (left), by moving the midpoint (middle), as layered mesh (right)

Consequently, the auxiliary meshes get adapted to the local problems. This adaptation is inspired by Shishkin-meshes [156], see also [116, 123, 149], which are graded in such a way that boundary layers are resolved. Another mesh adaptation is to construct layered meshes. This can be achieved as follows. We compute again the point $\mathbf{z}_F + (1 - \vartheta)\kappa \mathbf{b}_F$, but this time, we move the edges created in $\mathscr{T}_1(F)$ that are parallel to ∂F towards the boundary ∂F such that all edges have the same distance to ∂F and one edge lies on the computed point, see Fig. 6.12 (right). In the numerical realization, we set $\vartheta = 0.25$ independent of the local Péclet numbers. Otherwise, the auxiliary triangulations $\mathscr{T}_l(F)$ degenerate in the computations for small $l = 1, 2, 3$ and large Péclet numbers. Furthermore, we only present the results for the first mentioned mesh adaptation technique since the computed values in the experiments differ slightly.

The solutions of the resulting systems of linear equations, coming from the SUPG formulation, with non-symmetric, sparse matrices are approximated with the help of the GMRES method, see [150]. As the stopping criterion, we use the reduction of the norm of the initial residual by a factor of 10^{-10}.

Another preprocessing step is the computation of the matrices arising from the local boundary integral formulations. Here, we use the BEM code developed in the PhD thesis by Hofreither [94], which is based on a fully numerical integration scheme described in [151]. The inversions of the local single-layer potential matrices $\mathbf{V}_{K,l}$ are performed with an efficient LAPACK [6] routine.

The assembling of the global stiffness matrix is performed element-wise as described in Sect. 6.2.4 utilizing the non-symmetric representation of the Steklov–Poincaré operator in the local stiffness matrices. The resulting system of linear equations, which is again sparse and non-symmetric, is solved by GMRES. For the global problem, however, we use the reduction of the norm of the initial residual by a factor of 10^{-6} as the stopping criterion. In our numerical experiments, the GMRES iterations are carried out without preconditioning in general. However, we also implemented a simple diagonal preconditioner, namely a geometric row scaling

(GRS) preconditioner, see [86], with matrix

$$C^{-1} = \operatorname{diag}(1/\|B_j\|_p) \ ,$$

where by B_j we mean the j-th row of the global stiffness matrix, and we choose the vector norm with $p = 1$.

The proposed method is highly parallelizable, especially the preprocessing steps. The two-dimensional convection-diffusion-reaction problems on the faces are independent of each other, and can thus be treated in parallel. The subsequent setup of the boundary integral matrices and of $D_K^\top S_{K,l} D_K$ can be parallelized on an element level as well. Even the computations of the single entries of each boundary integral matrix are independent of each other.

In the implementation we use another observation to reduce the computational complexity. In the case of constant convection, diffusion and reaction terms, the local boundary integral matrices and the problems on the edges and faces are identical for elements which differ by some translation only. Therefore, we build a lookup table in a preprocessing step such that redundant computations are avoided.

Experiment 1

In the first numerical experiment, a problem with constant convection and diffusion terms is studied. Let $\Omega = (0, 1)^3$, and let us consider the boundary value problem

$$-\alpha \Delta u + \mathbf{b} \cdot \nabla u = 0 \quad \text{in } \Omega \ , \qquad u = g_D \quad \text{on } \Gamma \ ,$$

where $\mathbf{b} = (1, 0, 0)^\top$ and $g_D(\mathbf{x}) = x_1 + x_2 + x_3$. The domain Ω is discretized with tetrahedral elements, see Fig. 6.13. The discretization is constructed with the help of a uniform mesh with $8 \times 8 \times 8$ small cubes where each cube is split into 6 tetrahedra. Thus, the mesh consists of 3072 elements, 6528 faces, 4184 edges and 729 nodes

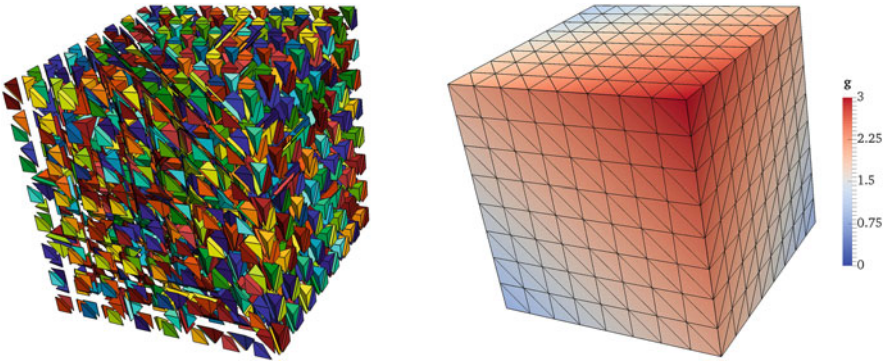

Fig. 6.13 Visualisation of tetrahedral mesh and Dirichlet data for Experiment 1

of which 343 nodes lie in the interior of Ω. Consequently, the number of degrees of freedom in the BEM-based FEM is equal to 343 in this example. The maximal element diameter is $h \approx 0.22$. The mesh is chosen rather coarse, but it is well suited for the study of stability.

Since the convection and diffusion parameters are constant over the whole domain, the lookup table is applied to speed up the computations. Instead of the before mentioned numbers of geometrical object, we only have to treat 6 elements, 12 faces and 7 edges in the preprocessing step, where the traces of the basis functions are computed and the local stiffness matrices are set up.

To handle the Dirichlet boundary condition, we apply pointwise interpolation of the data g_D to obtain an extension into Ω. The interpolant is bounded by 0 from below and by 3 from above on Γ. The convection-diffusion problem satisfies the maximum principle [82, 140], and therefore, we know that $0 \leq u \leq 3$ everywhere for the exact solution. To study stability of the BEM-based FEM, the maximum principle is checked for the approximate solution $u_{h,l} \in V_{h,l}$ obtained by (6.37). Since the basis functions satisfy convection-diffusion problems on the faces and edges and since the maximum principle is also valid there, the maximal values of $u_{h,l}$ should by reached in the nodes of the mesh. However, because of oscillations coming from the SUPG method on the faces, the maximal values might be found at some auxiliary node. Consequently, the maximum principle is tested on the whole skeleton Γ_S.

Table 6.3 gives a comparison of the classical finite element method with continuous piecewise linear basis functions and without stabilization, the original BEM-based FEM proposed in [96] with linear basis functions on the faces and the hierarchical, convection-adapted BEM-based FEM with $l = 2$ discussed in this chapter. The classical FEM satisfies the discrete maximum principle until

Table 6.3 Verifying maximum principle in Experiment 1

		Classic FEM		BEM-based FEM			
				Original [96]		Hierarchical, $l = 2$	
α	Pe_h	$u_{\min}$	$u_{\max}$	$u_{\min}$	$u_{\max}$	$u_{\min}$	$u_{\max}$
1.0×10^{-1}	2	0.00	3.00	0.00	3.00	0.00	3.00
5.0×10^{-2}	4	0.00	3.00	0.00	3.00	0.00	3.00
2.5×10^{-2}	9	0.00	3.00	0.00	3.00	0.00	3.00
1.0×10^{-2}	22	−0.55	3.00	0.00	3.00	−0.01	3.00
5.0×10^{-3}	43	−1.14	3.00	0.00	3.00	−0.01	3.00
2.5×10^{-3}	87	−1.85	3.07	0.00	3.00	−0.01	3.00
1.0×10^{-3}	217			0.00	3.00	−0.01	3.00
5.0×10^{-4}	433			0.00	3.00	−0.01	3.00
2.5×10^{-4}	866			−142.89	399.06	−0.01	3.00
1.0×10^{-4}	2165			−68.85	41.00	−0.01	3.00
5.0×10^{-5}	4330					−0.01	3.08
2.5×10^{-5}	8660					−0.01	14.72

$\alpha = 2.5 \times 10^{-2}$, which corresponds to a Péclet number of 9. The BEM-based strategies, which incorporate the behaviour of the differential operator into the approximation space, are more stable. The method in [96] passes the test up to $\alpha = 5.0 \times 10^{-4}$, which corresponds to $\mathrm{Pe}_h = 433$. In the new, proposed method we might have oscillations occurring in the approximation of the basis functions satisfying convection-dominated problems on the faces. If we neglect these small deviations in the third digit after the decimal point, the proposed method reaches even $\alpha = 1.0 \times 10^{-4}$, i.e. $\mathrm{Pe}_h = 2165$, for $l = 2$ without violation of the maximum principle.

Next, we study the influence of the auxiliary triangulations of the faces on the convection-adapted BEM-based FEM. In Table 6.4, the minimal and maximal values $u_{\min}$ and $u_{\max}$ of the approximate solution are listed for different levels l of the auxiliary meshes. The higher l is chosen, the longer the discrete maximum principle is valid. For $l = 3$, we even have stability until $\alpha = 2.5 \times 10^{-5}$, i.e. $\mathrm{Pe}_h = 8660$. The enhanced stability can be explained by the improved approximations of the boundary value problems on the edges and faces used to construct the basis functions. Obviously, the local oscillations in the construction of basis functions are reduced such that they have less effect to the global approximation.

In Table 6.4, the number of GMRES iterations are given without preconditioning. The GMRES solver for the proposed BEM-based FEM converges faster than for the preceding scheme. For increasing l the convergence slightly improves. Furthermore, the iteration numbers stay bounded without the help of any preconditioning until the maximum principle is violated.

Experiment 2

In this numerical experiment, we compare the convection-adapted BEM-based FEM with a well established method for convection-dominated problems, namely the Streamline Upwind/Petrov–Galerkin (SUPG) finite element method. The three-dimensional SUPG formulation is analogous to (6.33) and the stabilization parameter is chosen according to (6.40). The implementation has been done in the software `FreeFem++`, see [89]. For the comparison, we solve again the problem given in Experiment 1 with the BEM-based FEM and the SUPG method on the coarse tetrahedral discretization. Both approximations have 343 degrees of freedom. Furthermore, a reference solution is computed by the SUPG method on a fine tetrahedral mesh constructed with the help of $128 \times 128 \times 128$ cubes.

Having a closer look at the considered problem, we decompose the boundary of $\Omega = (0,1)^3$ into the inflow boundary, the outflow boundary and the characteristic boundary which are given by

$$\Gamma_{\mathrm{in}} = \{0\}\times(0,1)\times(0,1)\,, \quad \Gamma_{\mathrm{out}} = \{1\}\times(0,1)\times(0,1)\,, \quad \Gamma_{\mathrm{ch}} = \partial\Omega\setminus(\Gamma_{\mathrm{in}}\cup\Gamma_{\mathrm{out}})\,,$$

respectively. It is known, that the solution has an exponential layer near Γ_{out} and a characteristic/parabolic layer near Γ_{ch} in the convection-dominated regime, see [149]. The hierarchical construction of the basis functions for the BEM-based FEM is adapted to the exponential layers but not necessarily to the parabolic

Table 6.4 Verifying maximum principle and comparing GMRES-iterations in Experiment 1 for different mesh levels $l = 1, 2, 3$

		$l = 1$			$l = 2$			$l = 3$		
α	Pe_h	$u_{\min}$	$u_{\max}$	Iter.	$u_{\min}$	$u_{\max}$	Iter.	$u_{\min}$	$u_{\max}$	Iter.
5.0×10^{-3}	43	-0.01	3.00	28	-0.01	3.00	25	0.00	3.00	23
2.5×10^{-3}	87	-0.01	3.00	28	-0.01	3.00	26	0.00	3.00	24
1.0×10^{-3}	217	-0.01	3.00	28	-0.01	3.00	26	0.00	3.00	24
5.0×10^{-4}	433	-0.01	3.00	28	-0.01	3.00	25	0.00	3.00	23
2.5×10^{-4}	866	-0.01	3.00	28	-0.01	3.00	24	0.00	3.00	23
1.0×10^{-4}	2165	-0.01	5.19	30	-0.01	3.00	24	0.00	3.00	23
5.0×10^{-5}	4330	-6.72	169.93	49	-0.01	3.08	25	0.00	3.00	23
2.5×10^{-5}	8660	-4.8×10^{6}	1.3×10^{7}	302	-0.01	14.72	31	0.00	3.00	23
1.0×10^{-5}	21,651				-7.3×10^{3}	3.1×10^{4}	92	0.00	26.11	29
5.0×10^{-6}	43,301							-14.89	36.25	55

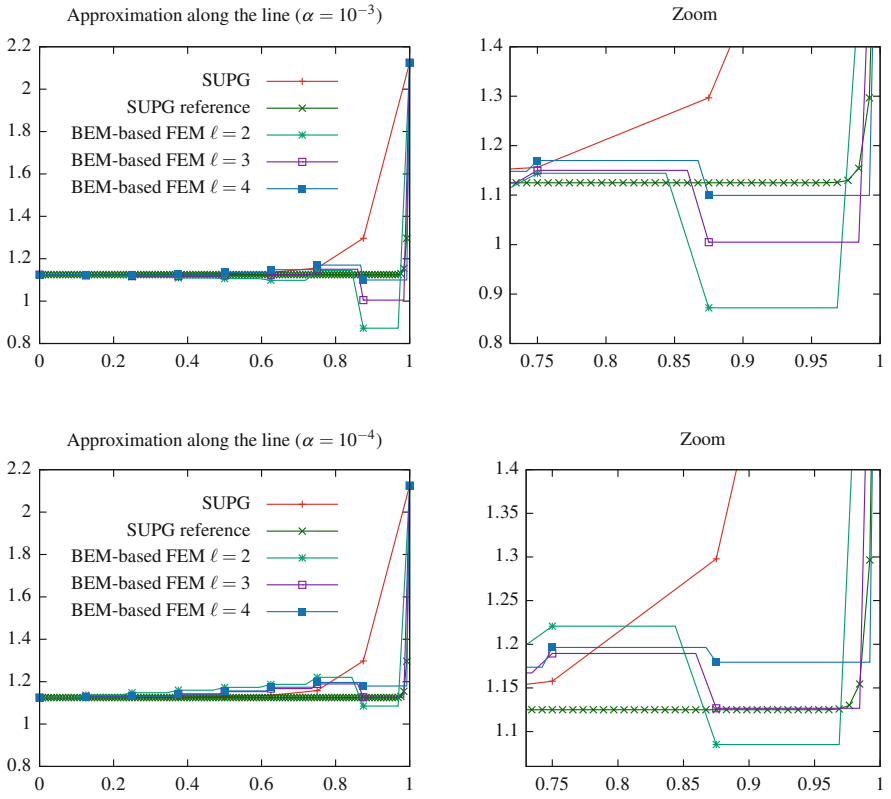

Fig. 6.14 Comparison of convection-adapted BEM-based FEM and SUPG approximation

layer because of the following reason: When we derived the local boundary value problems on the edges, faces and elements, we incorporate the behaviour in the direction of the convection, but we neglect the behaviour orthogonal to the faces, and thus, along the characteristic layer. Consequently, we should study exponential layers to see the advantages of the BEM-based FEM. Therefore, we compare the approximations along the line $s \mapsto (s, 5/8, 1/2)^\top$ for $s \in [0, 1]$, which is far from the characteristic boundary and which is aligned with edges of the discretization.

In Fig. 6.14, we give the approximations of the BEM-based FEM for different levels of the auxiliary triangulations of the faces, the SUPG approximation and the reference solution for $\alpha = 10^{-3}$ ($\mathrm{Pe}_h = 217$) and $\alpha = 10^{-4}$ ($\mathrm{Pe}_h = 2165$). The degrees of freedom are visualized by marks. The SUPG method shows no oscillations, but the layer in the solution is smeared out due to the stabilization. The SUPG approximations for $\alpha = 10^{-3}$ and $\alpha = 10^{-4}$ hardly differ although the layer in the solution changes. The convection-adapted BEM-based FEM has no explicit stabilization, and thus, we recognize some oscillations near the exponential layer. However, the layer is resolved much better with the same number of degrees of

freedom. Additionally, we have the possibility to improve the accuracy of the shape functions within the BEM-based FEM by increasing the level l, i.e., by refining the auxiliary triangulations of the faces. Doing this, the oscillations near the exponential layer are reduced and we obtain very accurate solutions for the global problem with only a few degrees of freedom. If we have a closer look at the plots in the right column of Fig. 6.14 with the details near the exponential layer, the curves indicate that the layer of the solution is already smeared out for the reference solution computed with the SUPG method on a very fine mesh.

Experiment 3

In the final numerical experiment, we consider a convection-diffusion problem with non-constant convection vector. In order to compare the experiments, let $\Omega = (0, 1)^3$. We solve

$$-\alpha \Delta u + \mathbf{b} \cdot \nabla u = 0 \quad \text{in } \Omega\,, \qquad u = g_D \quad \text{on } \Gamma\,,$$

where

$$\mathbf{b}(\mathbf{x}) = \frac{0.85}{\sqrt{(1-x_1)^2 + (1-x_3)^2}} \begin{pmatrix} x_3 - 1 \\ 0 \\ 1 - x_1 \end{pmatrix}$$

and g_D is chosen such that it is piecewise bilinear and continuous with $0 \leq g_D \leq 3$ on one side of the unit cube and zero on all others, see Fig. 6.15. The convection vector $\mathbf{b}$ is scaled in such a way that the Péclet numbers in the computations are comparable with those of Experiment 1. The convection is a rotating field around the upper edge of the unit cube Ω, which lies in the front when looking at Fig. 6.15.

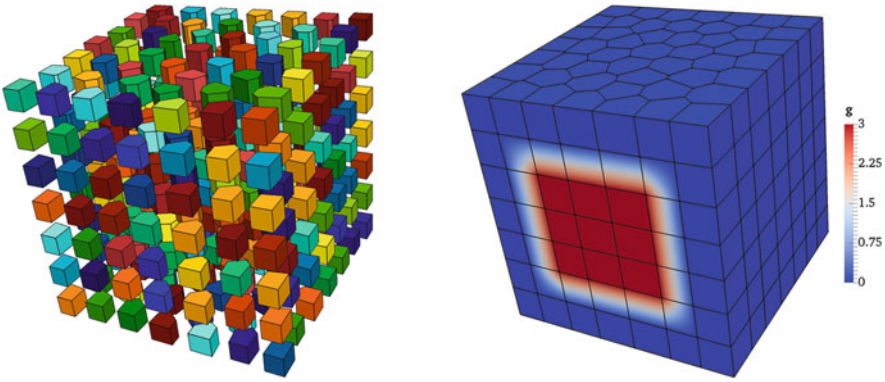

Fig. 6.15 Visualisation of polyhedral mesh and Dirichlet data for Experiment 3

Consequently, we expect that the non-zero Dirichlet data is transported towards the upper side of the cube for low diffusion.

This time, the domain Ω is decomposed into prisms having general polygonal ends, see Fig. 6.15. The polyhedral mesh consists of 350 elements, 1450 faces, 1907 edges and 808 nodes of which 438 nodes lie in the interior of Ω. Thus, the number of degrees of freedom in the BEM-based FEM is equal to 438. The maximal diameter of the elements is $h \approx 0.25$ and the discretization was chosen such that h is approximately the same as in Experiment 1.

In our experiment, the polyhedral mesh has less elements, faces and edges than the tetrahedral discretization. This is beneficial concerning the computations in the preprocessing step. Less local problems have to be solved on edges and faces and there are less boundary element matrices which have to be set up. Furthermore, polyhedral discretizations admit a high flexibility while meshing complex geometries. In Table 6.5, we list the minimal and maximal values of the approximation $u_{h,l}$ on the skeleton for $l = 2$ to verify the discrete maximum principle. Furthermore, the number of GMRES iterations are given with and without GRS preconditioning.

The first observation is that the number of GMRES iterations increases when the diffusion α tends to zero. Thus, the iteration count is not bounded in this experiment. However, this behaviour correlates with the violation of the maximum principle and is therefore the result of inaccuracies. Already with the help of the simple geometric row scaling preconditioner, we overcome the increase of the iteration number.

A more detailed discussion is needed for the discrete maximum principle. In Table 6.5, we observe that this principle is violated in a relatively early stage for $\alpha = 2.5 \times 10^{-2}$, which corresponds to $\mathrm{Pe}_h = 9$. However, the increase of $u_{\max}$ and the decrease of $u_{\min}$ is fairly slow for increasing Péclet number.

Table 6.5 Verifying maximum principle in Experiment 3 for $l = 2$ and number of iterations with/without preconditioning

α	Pe_h	$u_{\min}$	$u_{\max}$	Iter.	Iter. (prec.)
1.0×10^{-1}	2	0.00	3.00	20	20
5.0×10^{-2}	4	0.00	3.00	20	21
2.5×10^{-2}	9	0.00	3.04	20	21
1.0×10^{-2}	22	0.00	3.07	23	22
5.0×10^{-3}	43	−0.01	3.26	29	23
2.5×10^{-3}	86	−0.04	3.37	42	24
1.0×10^{-3}	216	−0.10	3.38	45	23
5.0×10^{-4}	431	−0.13	3.45	48	22
2.5×10^{-4}	863	−0.15	3.51	51	21
1.0×10^{-4}	2157	−0.15	3.53	52	21
5.0×10^{-5}	4313	−0.16	3.57	58	23
2.5×10^{-5}	8627	−0.25	4.38	69	28

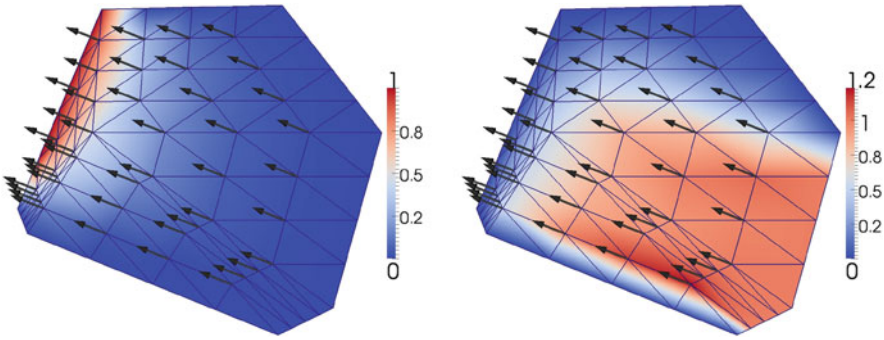

Fig. 6.16 Approximations of basis functions on polygonal face, projected convection vector and auxiliary triangulation with appropriately (left) and not appropriately (right) resolved boundary layer

Here, one has to point out that the computations are done on a polyhedral mesh with a globally continuous approximation $u_{h,l}$. This, by itself, is a current field of research even without dominant convection, see [28]. The geometry of polygonal faces is more complex than the triangles in Experiment 1, and thus, the computations on the faces are more involved.

Figure 6.16 presents the approximation of two different basis functions over the same polygonal face, the auxiliary triangulation and the projected convection vector. We can see how the local mesh has been adapted to the underlying differential operator, namely by moving the node, which lay initially in the center of the polygon, into the direction of the convection. In certain constellations, the boundary layers are not resolved appropriately. In the left picture of Fig. 6.16, the approximation of the basis function is satisfactory. In the right picture, however, oscillations occur in the lower right corner due to the relatively large triangles near the boundary. In many cases these situations are already resolved quite well by the simple mesh adaptation. When we introduced the moving of the auxiliary nodes in the implementation, the numerical results improved. Thus, we expect that a better adaptation of the local meshes, and consequently a better approximation of the local problems, improves the stability of the BEM-based FEM such that we would obtain comparable results to Experiment 1 for the discrete maximum principle.

Finally, in Fig. 6.17, the approximation $u_{h,l}$ is visualized for $l = 2$ and two different values of diffusion $\alpha = 2.5 \times 10^{-2}$ and $\alpha = 5.0 \times 10^{-5}$. The domain Ω has been cut through, such that the approximation is visible on a set of polygonal faces which lie in the interior of the domain. The expected behaviour of the solution can be observed. The Dirichlet data is transported into the interior of the domain along the convection vector. In the case of the convection-dominated problem, oscillations appear near the outflow boundary.

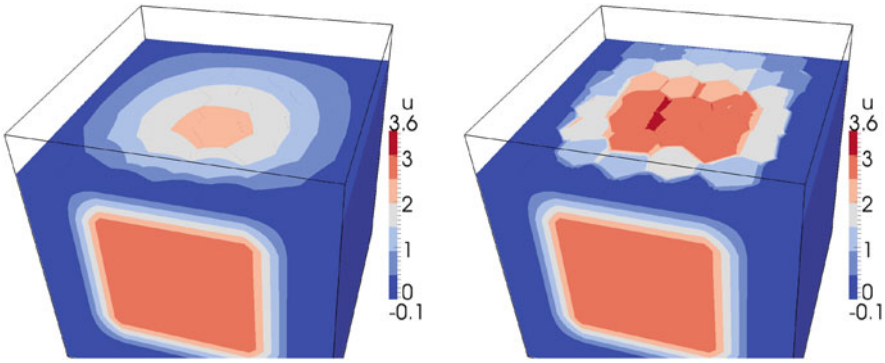

Fig. 6.17 Cut through the domain $\Omega = (0, 3)^3$ and visualisation of the approximation in Experiment 3 for $\alpha = 2.5 \times 10^{-2}$ (left) and $\alpha = 5.0 \times 10^{-5}$ (right)

Conclusion on Convection-Adapted BEM-Based FEM

We have derived convection-adapted BEM-based FEM discretization schemes for convection-diffusion-reaction boundary value problems that considerably extend the range of applicability with respect to the strength of convection. The numerical results have not only confirmed this enhanced stability property of the discretization scheme, but have also indicated faster convergence of the GMRES solver in comparison with the original BEM-based FEM scheme presented in [94, 96]. When compared to the SUPG method, our proposed method shows an improved resolution of the exponential layer at the outflow boundary.